Chaos ARTICLE pubs.aip.org/aip/cha

Synchronization and decoherence in a self-excited inertia-wheel multiple rigid-body dynamical system

Cite as: Chaos 33, 123107 (2023); doi: 10.1063/5.0151118
Submitted: 18 March 2023 · Accepted: 9 November 2023 ·
Published Online: 4 December 2023

G. Yakir[a] and O. Gottlieb[b]

AFFILIATIONS

Technion, Israel Institute of Technology, Haifa 3200003, Israel

[a]**Electronic mail:** gilad.yakir@epfl.ch
[b]**Author to whom correspondence should be addressed:** oded@technion.ac.il

ABSTRACT

We investigate the synchronization and decoherence of a self-excited inertia wheel multiple rigid-body dynamical system. We employ an Euler–Lagrange formulation to derive a nondimensional state space that governs the dynamics of a coupled pendula array where each element incorporates an inertia wheel. The dynamical system exhibits multiple equilibria, periodic limit-cycle oscillations, quasiperiodic, and chaotic oscillations and rotations. We make use of a combined approach including a singular perturbation multiple time scale and numerical bifurcation methodologies to determine the existence of synchronized and decoherent solutions in both weakly and strongly nonlinear regimes, respectively. The analysis reveals that synchronous oscillations are in-phase, whereas quasiperiodic oscillations are anti-phase. Furthermore, the non-stationary rotations are found to exhibit combinations of oscillations and rotations of the individual elements that are asynchronous. A Kuramoto order parameter analysis of representative solutions in various bifurcation regimes reveals the existence of chimera-like solutions where two elements are synchronized, whereas the third is desynchronized. Moreover, synchronous solutions were found to coexist with stable chimera solutions with a constant phase difference between the oscillators.

During the last two decades, there has been a growing interest in the stability and robustness of continuous and intermittent synchronization of periodic and nonstationary oscillations that have been observed in controlled experiments of mechanical networks. Some examples of synchronization in rigid-body and continuous dynamical systems have been documented for coupled mechanical metronomes,[1] coupled pendula suspended from a moving beam,[2] and a nanomechanical cantilever array.[3] Theoretical models for coupled metronome system experiments that exhibit synchronization of periodic limit-cycle oscillations incorporate generating self-excited escapement mechanisms that are based on a phenomenological van der Pol oscillator[4] or on impulsive forcing.[5] An alternative mechanism, for the generation of periodic limit cycles in a rigid body dynamical system, is an inertia (or reaction) wheel where self-excited oscillations are governed by controlling the torque via a coupled electrodynamic motor.[6] In order to resolve the complexity of synchronous and asynchronous self-excited oscillations in a mechanical network, we consistently model a multibody dynamical system and employ a combined analytical and numerical approach to investigate its self-excited dynamics. The theoretical analysis includes (i) the derivation of a coupled multibody dynamical system that incorporates inertia wheel feedback control for optimal self-excited operation; (ii) the asymptotic multiple-scale analysis of the weakly nonlinear configuration for the dynamical system where a set of slowly varying evolution equations enable a stability analysis of synchronous oscillations; and (iii) the numerical analysis of a strongly nonlinear configuration where in-phase (IP), anti-phase (AP), and chimera-like (CL) states can coexist augmented by global homoclinic bifurcations. The significance of this research is twofold. First, the proposed combined analytical and numerical methodologies will enable consistent identification of local and global stability thresholds of the multibody system for both weakly and strongly nonlinear ranges of operation, respectively. Second, the combined methodologies enable the construction of a comprehensive nonlinear bifurcation structure, incorporating

alternative feedback laws for optimal self-excited oscillation stabilization in mechanical networks.

I. INTRODUCTION

An inertia wheel pendulum (IWP) is a simple pendulum augmented by a rotating wheel at its end and was first introduced by Spong, Block, and Åström.[7] The coupling torque between the wheel and the pendulum can be used to control the motion of the pendulum. Although this device exhibits relatively simple dynamic properties, it also obtains several interesting properties such as underactuation, which stems from the fact that it has two degrees of freedom with only one actuator, and nonlinearity, since the dynamics are described by an oscillating pendulum.[6] The IWP is, therefore, an intriguing and classical testbed used to study new control strategies such as the design of a robust controller for the stabilization of the inverted IWP[8] and novel mechatronic systems that utilize an inertial wheel for their dynamics, for example, the stabilization of a wheel-robot.[9]

To control this unstable nonlinear plant, a control action capable of dominating the gravity torque is required. An effective solution to this constraint implements a hybrid-type strategy in which a dual controller method is applied. First, a nonlinear controller is used to swing up the pendulum to an inverted position, and then a linear controller is used for local stabilization at the inverted position; this scheme has been successfully enacted in many types of inverted pendula problems.[10–12] A less intuitive method to swing up and reach stability at the inverted position uses methods from bifurcation theory and energy-type considerations to construct a bounded continuous control law.[13,14] We apply a bounded continuous control law globally to coupled pendula in two spring-coupled arrays to study the non-stationary dynamics and synchronization within this mechanical network. In our system, the controller does not serve any specific objective function as it would in most mechanical systems. Rather it acts within the dynamical system to destabilize it from its zero equilibrium and produce different dynamical behaviors.

Spontaneous synchronization is encountered in various fields of science, engineering, and social behavior.[15,16] Examples are endless, and some well-known ones include the self-excited resonant vibrations of the London's pedestrian-crowded Millennium Bridge.[17] This response was caused when the pedestrians' footsteps spontaneously synchronized with the vibrations of the bridge, therefore amplifying them. Another common example is the synchronous flashing of fireflies in Southeast Asia. Male fireflies are known to emit rhythmic light pulses in order to attract females and are able to synchronize their flashes with their neighbors. In fact, for 300 years, travelers to Southeast Asia had been witnessing and detailing large swarms of fireflies blinking on and off in unison. This began to be recorded in scientific journals by the beginning of the 20th century and was made famous within the mathematics community when Mirollo and Strogatz[18] suggested a simple model of episodic and pulse-like interactions to explain this phenomenon. Although the first example of spontaneous synchronization was first reported in the 17th century, a few centuries went by before this was to be formulated mathematically. The first to do so was Yoshiki Kuramoto,[19] what he suggested is known today as the Kuramoto model. This model allowed for a breakthrough in the study of synchronization in coupled oscillators since it enables a simple measure of the degree of synchronization within a system. Applying this model together with the Hilbert transform[20] allows us to numerically analyze the synchronous dynamics of the IWP array.

In mechanical networks, synchronous dynamics occur when there exists a sufficiently weak coupling strength within the system. Theoretical explanations for this phenomenon have been proposed since the last century.[21] More recently, some studies have set out to explain this phenomenon by exploring the parameter space of synchronized identical simple oscillators that interact through a common support.[22,23] While other studies have suggested control laws to control the synchronous oscillations of systems ranging from coupled pendula[24,25] to hierarchical networks of coupled oscillators.[26] However, unlike these simple oscillators, constructing an accurate model of a system of coupled metronomes is challenging because of the complex escapement mechanism within the metronomes. Consequently, such models commonly incorporate nonlinear terms to describe the operation of the escapement, such as a nonlinear van der Pol type damping term[27] or a discontinuous impulse function[5,28] that provides a higher degree of realism to describe the escapement mechanism of the metronome or clock.[29] In the IWP array, a continuous model is constructed directly from the rigid body mechanics of the system. The self-excited oscillations in the proposed system arise not because of the common van der Pol type damping applied to similar pendula systems[30] but rather because of a continuous underactuating controller common to many engineering systems. We note that the dynamics of the aforementioned mechanical networks were limited to periodic oscillations. We propose a network capable of periodic, quasiperiodic, and chaotic dynamics. Rather unintuitively chaotic systems may (*i*) be controlled and (*ii*) synchronize.[31,32] Control of chaos is essentially a tracking problem in which one designs a controller that guarantees that regardless of the initial conditions the closed-loop controlled system converges to a specified trajectory within the chaotic attractor. A solution to this tracking problem was detailed by Ott, Grebogi, and Yorke, which is now known as the OGY method.[33] Synchronization in chaos implies that despite the sensitive dependence on initial conditions the state error between two chaotic systems goes to zero. Recent developments allow for fast experimental determination of these synchronous domains[34] in real-world systems, and experimental studies have shown the existence of synchrony within chaotic coupled pendula[35] and rotating double pendula systems.[36] The literature on control of synchronization is abundant. However, as the focus of this work is on the dynamical systems perspective to the transition from synchronization to decoherence (and its possible bifurcation structure with chimera-like solutions), we have not elaborated on multiple alternatives to control synchronization.

The paper is organized as follows: In Sec. II, we formulate the nondimensional autonomous system and its state space representation. In Sec. III, we conduct a linear stability analysis of the zero equilibrium. Section IV contains an asymptotic analysis of the synchronized dynamics of the IWP array. This includes the implementation of the method of multiple scales to formulate an existence criterion for IP synchronization. A comprehensive bifurcation diagram is constructed via continuation methods in Sec. V.

The Kuramoto order parameter is then derived and used to study the synchronous states of the system numerically. We summarize our results in Sec. VI.

II. PROBLEM FORMULATION

A. Equations of motion

An IWP array is composed of three IWPs coupled by a beam (1). An Euler–Lagrange approach is implemented to formulate the dynamical system, where the system energies are that of the beam, rods, pendulums, and wheels, leading to the system kinetic and potential energies being formulated in Eqs. (1) and (2), respectively, under the assumption of inextensibility of the rigid-body elements of the dynamical system portrayed in Fig. 1,

$$\begin{aligned} \mathrm{KE}_{p,k} &= \frac{1}{2}\left[m_p\left(v_{p,k}\right)^2 + I_{p,cm}\left(\dot{\theta}_k\right)^2\right], \\ \mathrm{KE}_{w,k} &= \frac{1}{2}\left[m_w\left(v_{w,k}\right)^2 + I_{w,cm}\left(\dot{\phi}_k + \dot{\theta}_k + \dot{\psi}\right)^2\right], \\ \mathrm{KE}_{\psi} &= \frac{1}{2}\left[m_{\psi}\left(v_{\psi}\right)^2 + I_{\psi,cm}\left(\dot{\psi}\right)^2\right], \\ \mathrm{KE}_{b} &= \frac{1}{2} m_b\left(v_b\right)^2 + I_b\left(\dot{\psi}\right)^2, \end{aligned} \tag{1}$$

$$\begin{aligned} \mathrm{PE}_{p,k} &= m_p\left[l_{\psi}\left(1-\cos\psi\right) + l_p\left(1-\cos\theta_k\right)\right]g, \\ \mathrm{PE}_{w,k} &= m_w\left[l_{\psi}\left(1-\cos\psi\right) + l_w\left(1-\cos\theta_k\right)\right]g, \\ \mathrm{PE}_{\psi} &= m_{\psi}\left[l_{\psi,cm}\left(1-\cos\psi\right)\right]g, \\ \mathrm{PE}_{b} &= m_b\left[l_{\psi}\left(1-\cos\psi\right)\right]g. \end{aligned} \tag{2}$$

The subscripts p, w, ψ, and b represent the pendulum, wheel, rod, and beam, respectively; $k = i-1, i, i+1$ indicates the location of the oscillator from left to right. The velocities $v_{p,k}$, $v_{w,k}$, $v_{\psi,k}$, and $v_{b,k}$ and full derivation of the system energies can be found in Appendix A. The system generalized forces,

$$\begin{aligned} Q_{\psi} &= -D_{\psi}\,\dot{\psi}, \\ Q_{p} &= -D_{\theta}\,\dot{\theta}_k, \\ Q_{w} &= \left(\tau_k - D_{\phi}\,\dot{\phi}_k\right), \end{aligned} \tag{3}$$

include a damping term obtained with a Rayleigh's dissipation function with dissipation constants D_{ψ}, D_{θ}, $andD_{\phi}$ for each oscillating element of the system. Energy enters the system by means of a torque applied by a DC-motor to each wheel. There is no external forcing applied to the system, thus yielding a system of self-excited oscillators. The simplified but commonly used model of a DC motor in Eq. (4) includes the motor-to-disk reduction ratio N, the rotor coil resistance R, a torque constant k_m, and a back electromotive force (EMF) constant k_p. The control voltage $V_{j,k} = G_1 \sin\theta_k + G_2\dot{\theta}_k + G_3\dot{\phi}_k$[14] is a partial state feedback, thus forming an underactuated system with control gains G_i,

$$\tau_k = \left(N k_m/R\right)\left[G_1 \sin\theta_k + G_2\dot{\theta}_k + \left(G_3 - N k_p\right)\dot{\phi}_k\right]. \tag{4}$$

This control law is one of the many alternatives that can be employed for underactuated control systems. Although simple and straightforward, it allows us to study the synchronous dynamics that arise from self-excitation using purely physics-based modeling without the need for phenomenological terms to describe the system dynamics. This, in turn, allows us to explore synchronization in mechanical systems beyond the expected periodic limit-cycle oscillations. Using Eqs. (1)–(4), we construct the Lagrangian function $\mathscr{L} = \mathrm{KE} - \mathrm{PE}$ and arrive at the Euler–Lagrange equations of motion,

$$d/dt\left(\partial\mathscr{L}/\partial\dot{\mathbf{q}}\right) - \partial\mathscr{L}/\partial\mathbf{q} = \mathbf{Q}^{NC}. \tag{5}$$

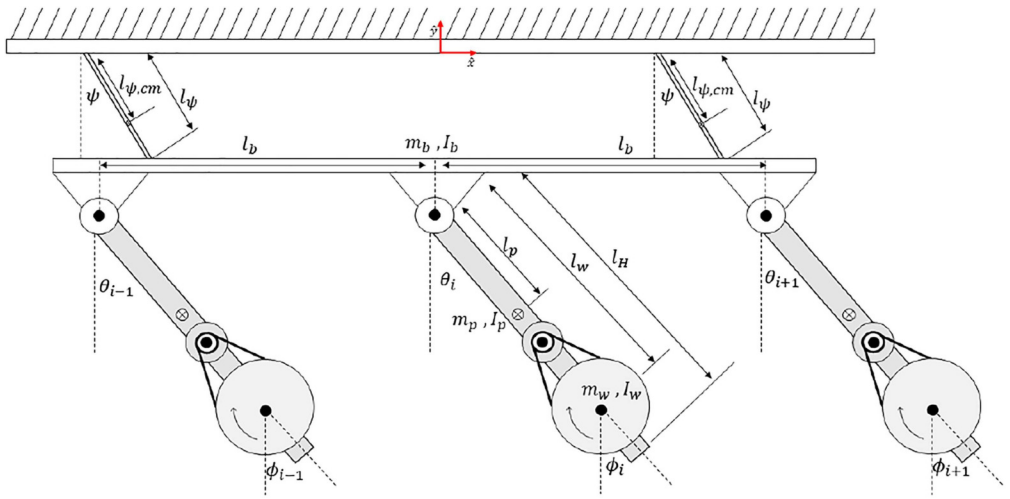

FIG. 1. Definition sketch of an IWP array.

With generalized coordinates,

$$\mathbf{q} = \begin{pmatrix} \psi & \theta_{i-1} & \theta_i & \theta_{i+1} & \phi_{i-1} & \phi_i & \phi_{i+1} \end{pmatrix}, \tag{6}$$

leading to the time-invariant nonlinear dynamical system,

$$\mathbf{M}\,\ddot{\mathbf{q}} = \mathbf{F}\left(\mathbf{q}, \dot{\mathbf{q}}\right), \tag{7}$$

where the mass and forcing matrices are

$$\mathbf{M} = \begin{pmatrix} I_{eq2} + 3I_w & \mathbf{m_{12}} & \mathbf{m_{13}} \\ (\mathbf{m_{12}})^T & (I_{eq1} + I_w)\cdot \mathbf{I_{3\times 3}} & I_w \cdot \mathbf{I_{3\times 3}} \\ (\mathbf{m_{13}})^T & I_w \cdot \mathbf{I_{3\times 3}} & I_w \cdot \mathbf{I_{3\times 3}} \end{pmatrix}, \tag{8}$$

$$\mathbf{F} = \begin{pmatrix} Q_\psi - R_2 \sin\psi - I_{eq3} \sum_{k=i-1}^{i+1} \left(\dot{\theta}_k\right)^2 \sin\Delta_k \\ Q_{\theta,i-1} + I_{eq3}\,\dot{\psi}^2 \sin\Delta_{i-1} - R_1 \sin\theta_{i-1} \\ Q_{\theta,i} + I_{eq3}\dot{\psi}^2 \sin\Delta_i - R_1 \sin\Delta_i \\ Q_{\theta,i+1} + I_{eq3}\dot{\psi}^2 \sin\Delta_{i+1} - R_1 \sin\theta_{i+1} \\ Q_{\phi,i-1} \\ Q_{\phi,i} \\ Q_{\phi,i+1} \end{pmatrix},$$

and

$$\begin{aligned} \mathbf{m_{12}} &= \begin{bmatrix} I_w + I_{eq3}\cos\Delta_{i-1} & I_w + I_{eq3}\cos\Delta_i & I_w + I_{eq3}\cos\Delta_{i+1} \end{bmatrix}, \\ \mathbf{m_{13}} &= I_w \cdot \begin{bmatrix} 1 & 1 & 1 \end{bmatrix}, \\ I_{eq1} &= l_w^2\, m_w + l_p^2\, m_p + I_p, \\ I_{eq2} &= \left[m_b + 3\,\left(m_p + m_w\right)\right]\, l_\psi^2 + 2\, m_\psi\, l_{\psi,cm}^2 + 2\, I_\psi, \\ I_{eq3} &= \left(l_p\, m_p + l_w\, m_w\right)\, l_\psi, \\ R_1 &= \left(m_w\, l_w + m_p\, l_p\right)\, g, \\ R_2 &= \left\{\left[m_b + 3\,\left(m_p + m_w\right)\right]\, l_\psi + 2\, m_\psi l_{\psi,cm}\right\}\, g, \\ \Delta_k &= \psi - \theta_k. \end{aligned} \tag{9}$$

B. Nondimensional state space

The nondimensional system is obtained by defining the nondimensional time scaling $\tau = t/T_s = \omega_s t$ and frequency $\omega_s = \sqrt{R_1/I_{eq1}}$. Applying this to Eq. (7), the nondimensional autonomous system

$$\hat{\mathbf{M}}\mathbf{q}_{\tau\tau} = \hat{\mathbf{F}}\left(\mathbf{q}, \mathbf{q}_\tau\right) \tag{10}$$

is formulated, where $d/d\tau$ represents the first nondimensional time derivative. The nondimensional mass and forcing matrices are given explicitly as

$$\hat{\mathbf{M}} = \begin{pmatrix} \mu_2 + 3\mu_w & \hat{\mathbf{m}_{12}} & \hat{\mathbf{m}_{13}} \\ \left(\hat{\mathbf{m}_{12}}\right)^T & \mu_1 \cdot \mathbf{I_{3\times 3}} & \mu_w \cdot \mathbf{I_{3\times 3}} \\ \left(\hat{\mathbf{m}_{13}}\right)^T & \mu_w \cdot \mathbf{I_{3\times 3}} & \mu_w \cdot \mathbf{I_{3\times 3}} \end{pmatrix}, \tag{11}$$

$$\hat{\mathbf{F}} = \begin{pmatrix} -\mu_3 \sum_{k=i-1}^{i+1} \sin\Delta_k \theta_{\tau,k}^2 - \kappa \sin\psi - \delta_\psi \psi_\tau \\ \mu_3 \sin\Delta_{i-1}\left(\psi_\tau\right)^2 - \sin\theta_{i-1} - \delta_{\theta,i-1}\theta_{\tau,i-1} \\ \mu_3 \sin\Delta_i \left(\psi_\tau\right)^2 - \sin\theta_i - \delta_{\theta,i}\theta_{\tau,i} \\ \mu_3 \sin\Delta_{i+1}\left(\psi_\tau\right)^2 - \sin\theta_{i+1} - \delta_{\theta,i+1}\theta_{\tau,i+1} \\ \Gamma_3\phi_{\tau,i-1} + \Gamma_2\theta_{\tau,i-1} + \Gamma_1 \sin\theta_{i-1} \\ \Gamma_3\phi_{\tau,i} + \Gamma_2\theta_{\tau,i} + \Gamma_1 \sin\theta_i \\ \Gamma_3\phi_{\tau,i+1} + \Gamma_2\theta_{\tau,i+1} + \Gamma_1 \sin\theta_{i+1} \end{pmatrix} = \begin{pmatrix} f_1 \\ f_2 \\ f_3 \\ f_4 \\ f_5 \\ f_6 \\ f_7 \end{pmatrix}.$$

We note that $f_{1,2,3,4}$ incorporate gyroscopic terms from kinetic energy, restoring forces from potential energy, and dissipation from a Rayleigh's function. Furthermore, $f_{5,6,7}$ incorporate nondimensional control torques augmented by the dissipation of the inertia wheel. This nondimensional system now includes nondimensional inertia parameters

$$\mu_1 = 1 + \mu_w \quad \mu_2 = \frac{I_{eq2}}{I_{eq1}} \quad \mu_3 = \frac{I_{eq3}}{I_{eq1}} \quad \mu_w = \frac{I_w}{I_{eq1}}, \tag{12}$$

nondimensional damping coefficients

$$\delta_\theta = D_\theta/R_1 \quad \delta_\psi = D_\psi/R_1, \tag{13}$$

and a ratio of gravitational potential energies $\kappa = R_2/R_1$. By defining the nondimensional control gains,

$$\begin{aligned} \Gamma_1 &= \frac{Nk_m}{R_1 R} G_1, \\ \Gamma_2 &= \frac{Nk_m}{R_1 R} G_2, \\ \Gamma_3 &= \frac{Nk_m\omega_s}{R_1 R}\left[G_3 - Nk_p - D_\phi \frac{R}{Nk_m}\right], \end{aligned} \tag{14}$$

we can examine the system dynamics with respect to control gain inputs. We define the state vector

$$\mathbf{x} = \begin{bmatrix} \boldsymbol{\psi} & \boldsymbol{\theta} & \boldsymbol{\phi} \end{bmatrix}^T, \tag{15}$$

where

$$\begin{aligned} \boldsymbol{\psi} &= \begin{bmatrix} \psi & \psi_\tau \end{bmatrix}, \\ \boldsymbol{\theta} &= \begin{bmatrix} \theta_{i-1} & \theta_{\tau,i-1} & \theta_i & \theta^{\tau,i} & \theta i+1 & \theta_{\tau,i+1} \end{bmatrix}, \\ \boldsymbol{\phi} &= \begin{bmatrix} \phi_{\tau,i-1} & \phi_{\tau,i} & \phi_{\tau,i+1} \end{bmatrix}. \end{aligned}$$

Taking the first nondimensional time derivative of the state vector $\mathbf{x}$, we find the state space representation

$$\mathbf{x}_\tau = \begin{bmatrix} x_2 & f_1 & x_4 & f_2 & x_6 & f_3 & x_8 & f_4 & f_5 & f_6 & f_7 \end{bmatrix}^T \tag{16}$$

of the IWP array. The values f_i are given in Appendix B. Note that the nondimensional system in Eq. (10) is governed by 10 nondimensional parameters, whereas the dimensional Eq. (7) is governed by 21 parameters.

C. Limiting cases

By fixing the far pendulums at

$$\theta_{i-1} = \theta_{i+1} = \phi_{i-1} = \phi_{i+1} = 0, \tag{17}$$

we obtain a single pendulum on an oscillating base. The state vector of the array can now be reduced to $\mathbf{x} \in \mathbb{R}^5$, and the nondimensional autonomous system in Eq. (10) is condensed to

$$\tilde{\mathbf{M}}\mathbf{q}_{\tau\tau} = \tilde{\mathbf{F}}(\mathbf{q}, \mathbf{q}_\tau), \tag{18}$$

where

$$\tilde{\mathbf{M}} = \begin{pmatrix} \mu_2 + \mu_w & \mu_w + \mu_3 \cos\Delta & \mu_w \\ \mu_w + \mu_3 \cos\Delta & \mu_1 & \mu_w \\ \mu_w & \mu_w & \mu_w \end{pmatrix},$$

$$\tilde{\mathbf{F}} = \begin{pmatrix} -\mu_3 \sin\Delta\theta_\tau^2 - \kappa \sin\psi - \delta_\psi \psi_\tau \\ \mu_3 \sin\Delta\psi_\tau^2 - \sin\theta - \delta_\theta \theta_\tau \\ \Gamma_3\phi_\tau + \Gamma_2\theta_\tau + \Gamma_1 \sin\theta \end{pmatrix} = \begin{pmatrix} \tilde{f}_1 \\ \tilde{f}_2 \\ \tilde{f}_3 \end{pmatrix}.$$

All nondimensional parameters μ_i remain unchanged apart from $\mu_2 = \tilde{I}_{eq2}/I_{eq1}$, which now accounts for one pendulum instead of three such that

$$\tilde{I}_{eq2} = \left(m_b + m_p + m_w\right) l_\psi^2 + 2m_\psi l_{\psi,cm}^2 + I_\psi.$$

The $\mathbf{x} \in \mathbb{R}^5$ state vector is given by

$$\tilde{\mathbf{x}} = \begin{pmatrix} \psi & \psi_\tau & \theta & \theta_\tau & \phi_\tau \end{pmatrix}^T \in \mathbb{R}^5; \tag{19}$$

thus, the state-space formulation is

$$\tilde{\mathbf{x}_\tau} = \frac{1}{\det\left(\tilde{\mathbf{M}}\right)} \begin{pmatrix} \tilde{x}_2 \det\left(\tilde{\mathbf{M}}\right) & \tilde{F}_1\mu_w & \tilde{x}_4 \det\left(\tilde{\mathbf{M}}\right) & \tilde{F}_2\mu_w & -\tilde{F}_3 \end{pmatrix}^T, \tag{20}$$

where

$$\tilde{F}_1 = \left(\tilde{f}_2 - \tilde{f}_3\right)\mu_2 + \left(\tilde{f}_3 - \tilde{f}_1\right)\mu_3 \cos\Delta,$$

$$\tilde{F}_2 = \tilde{f}_1 - \tilde{f}_3 + \left(\tilde{f}_3 - \tilde{f}_2\right)\mu_3 \cos\Delta,$$

$$\tilde{F}_3 = \tilde{f}_3\left[(\mu_w + \mu_2)\,\mu_1 - (\mu_3 \cos\Delta + \mu_w)^2\right] + \left[\tilde{f}_2\left(\mu_3 \cos\Delta - \mu_2\right) + \tilde{f}_1\left(\mu_3 \cos\Delta - 1\right)\right]\mu_w,$$

and the determinant of the mass matrix is

$$\det\left(\tilde{\mathbf{M}}\right) = \mu_w\left[\mu_2 - (\mu_3 \cos\Delta)^2\right].$$

A single element within the array reduces to the third-order dynamics of an inertia wheel pendulum. By zeroing the effects of the coupling beam and the oscillating rods, we obtain the nonlinear differential equations of a single inertia wheel pendulum,

$$\begin{pmatrix} \mu_1 & \mu_w \\ \mu_w & \mu_w \end{pmatrix} \mathbf{q}_{\tau\tau} = \begin{pmatrix} -\delta\theta_\tau - \sin\theta \\ \Gamma_1 \sin\theta + \Gamma_2\theta_\tau + \Gamma_3\phi_\tau \end{pmatrix}. \tag{21}$$

By defining the state vector $\mathbf{x} = \begin{pmatrix} \theta & \theta_\tau & \phi_\tau \end{pmatrix}^T$, we obtain the state-space representation

$$\mathbf{x}_\tau = \begin{pmatrix} x_2 \\ -(\Gamma_1 + 1)\sin\theta - (\Gamma_2 + \delta)\,\theta_\tau - \Gamma_3\phi_\tau \\ \left[(1 + 1/\mu_w)\,\Gamma_1 + 1\right]\sin\theta + \left[(1 + 1/\mu_w)\,\Gamma_2 + \delta\right]\theta_\tau + \Gamma_3\phi_\tau \end{pmatrix}. \tag{22}$$

We note that Γ_2 relates to the dissipation of energy from the system and, therefore, primarily controls the lengths of transients.

TABLE I. Estimated values of nondimensional parameters for the strongly nonlinear system.

$\mu_1 = 1.0369$	$\mu_2 = 0.5026$	$\mu_3 = 0.3552$	$\mu_w = 0.0369$
$R_1 = 2.4436$	$R_2 = 3.4742$	$\kappa = 1.4217$	

D. Estimation of parameters

Following an experiment conducted on the oscillations of coupled pendulums,[37,38] we derive an estimation of the physical dimensions of the system without the wheel. The length of the wheel from the pendulum base l_w is estimated by assuming the wheel is located at a three-quarters length of the pendulum. We note the system elements that are made of aluminum alloy 6061 (2700 [kg/m^3]) and find the masses and moments of inertia. All dimensional parameters are listed in Appendix C. These lead to nondimensional parameters of the strongly nonlinear system given in Table I. The weakly nonlinear system is analyzed for a different set of nondimensional parameters (this will be outlined in further depth in Sec. IV), and these parameters can be found in Table II.

III. EQUILIBRIUM ANALYSIS

A. Stability maps

The IWP array's zero equilibrium with respect to gains $\Gamma_3(\Gamma_1)$ is estimated numerically using orthogonal collocation by implementing the continuation software *MatCont*;[39,40] all free parameters used in *MatCont* are given in Table IV. We construct the stability map (Fig. 2) by obtaining Hopf bifurcation for discrete values of gains $\Gamma_3(\Gamma_1)$. The discrete values found in the simulations are indicated by bold points, and linear extrapolation is conducted between every two points. Furthermore, a Neimark–Sacker bifurcation threshold was found (blue-dashed), indicating the onset of another frequency of oscillations and producing a quasiperiodic

TABLE II. Estimated values of nondimensional parameters for the weakly nonlinear system.

$\mu_1 = 1.03$	$\mu_2 = 0.8$	$\mu_3 = 0.02$	$\mu_w = 0.03$	$\kappa = 0.95$

response. This method, however, is not to suggest that an analytical solution cannot be obtained. The method for obtaining an analytical expression for the Hopf bifurcation threshold is outlined in Appendix E by implementing the algorithm derived by Guckenheimer[41] on the IWP array. The analytical analysis of the zero equilibrium yields the characteristic polynomial $\sum_{n=0}^{11} c_n \lambda^n$; for our parameter set, we obtain the coefficients

$$\begin{aligned} c_0 &= -\det \mathbf{J}|_0 = -\mu_2^3(\mu_2 - 3\mu_3^2)^{-1}\kappa\Gamma_3^3, \\ c_1 &= \Gamma_3^2 \cdot f_1(\Gamma_1, \Gamma_3), \\ c_2 &= \Gamma_3 \cdot f_2(\Gamma_1, \Gamma_3), \end{aligned} \tag{23}$$

indicating that a saddle node at $\Gamma_3 = 0$ produces a codimension 2 triple zero bifurcation.

Figure 2 reveals areas in which the zero equilibrium is asymptotically stable (region I—red); this region then loses stability to a super-critical or sub-critical Hopf bifurcation (black-solid) for negative or positive values Γ_1, respectively. The subcritical Hopf bifurcation gives rise to a very narrow bistable region III_A and to the emergence of stable limit cycle oscillation (LCO) regions *II* and III_B. These LCOs lose stability via a Neimark–Sacker bifurcation (blue-dashed), and quasiperiodic oscillations are obtained. These eventually make way to chaotic oscillations and then to the rotational dynamics of the pendula. The strongly and weakly nonlinear systems produce similarly valued Hopf bifurcations. However, the sub-critical bifurcations observed for positive values of gain Γ_1 appear only in the strongly nonlinear system (Fig. 2—top).

B. Internal resonances

The solution for the seven natural frequencies of the IWP array produces three zero frequencies,

$$\omega_1 = \omega_2 = \omega_3 = 0. \tag{24}$$

Together with the three unique frequencies,

$$\begin{aligned} \omega_4 &= \omega_5 = \sqrt{\Gamma_1 + 1}, \\ \omega_6 &= \sqrt{\frac{\Gamma_1\mu_3\sum_{k=i-1}^{i+1}(\cos\Delta_k) - \mu_2(1+\Gamma_1) - \kappa + a_5}{2\left[\mu_3^2\sum_{k=i-1}^{i+1}(\cos^2\Delta_k) - \mu_2\right]}}, \\ \omega_7 &= \sqrt{\frac{\mu_2(1+\Gamma_1) + \kappa - \Gamma_1\mu_3\sum_{k=i-1}^{i+1}(\cos\Delta_k) + a_6}{2\left[\mu_3^2\sum_{k=i-1}^{i+1}(\cos^2\Delta_k) - \mu_2\right]}}, \end{aligned} \tag{25}$$

where a_i is given in Appendix F. The non-zero natural frequencies and their ratios with respect to gain Γ_1 are summarized in Fig. 3 for $\kappa = 1.42$. These produce a $3:1$ internal resonance at $\Gamma_1 \approx 0.5$ and a near $1:1$ internal resonance at $\Gamma_1 \approx 1$.

Furthermore, we obtain the natural frequencies $\omega_1 = \sqrt{b_5\kappa}$ and $\omega_2 = 1$ of the weakly nonlinear system (4) and exploit the $1:1$ internal resonance to formulate a detuning parameter in Sec. IV.

IV. ASYMPTOTIC ANALYSIS

We apply a singular perturbation approach using an asymptotic multiple scale analysis[42,43] to investigate the weakly nonlinear single array system.

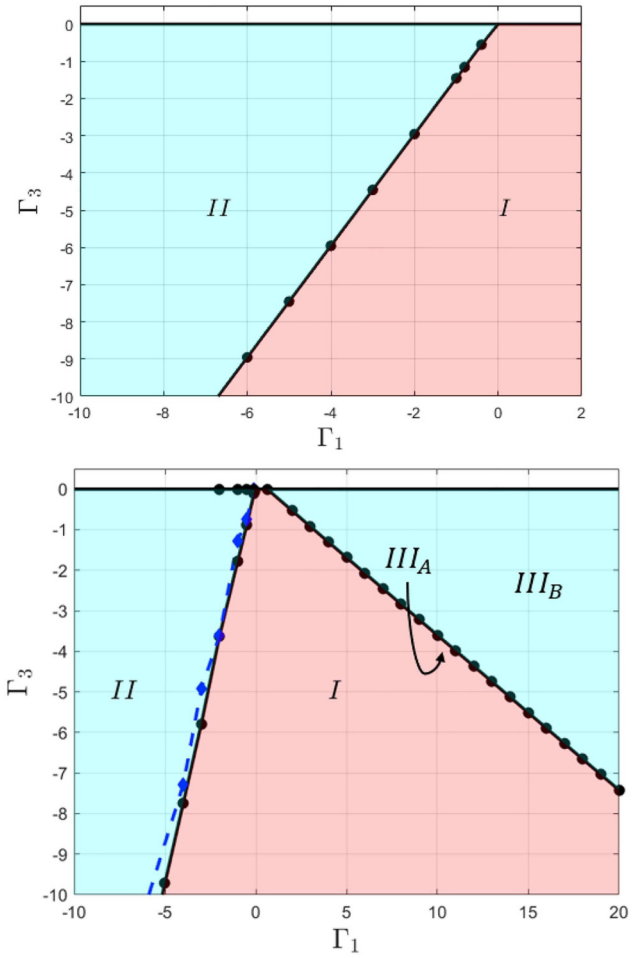

FIG. 2. Stability map of control gains $\Gamma_3(\Gamma_1)$ for the weakly (top) and strongly (bottom) nonlinear systems where region *I* (red) defines the parameter values for a stable equilibrium and regions *II* and *III* (blue) define the parameter values with possible limit cycles. The regions are separated by a Hopf threshold (solid black line).

A. Cubic order system

We find the cubic order dynamical equations of motion by expanding the transcendental functions in Eq. (10) about the stable equilibrium $\theta_k^* = \psi^* = 0$. This yields the approximated system

$$\underline{\mathbf{M}}\mathbf{q}_{\tau\tau} = \underline{\mathbf{F}}. \tag{26}$$

We note that the matrices $\underline{\mathbf{M}}$ and $\underline{\mathbf{F}}$ are given in Appendix G. For the purpose of simplification, we conduct an order analysis of the leading coefficients of the inertia variables. We can first assume that μ_w *and* μ_3 are of order $O(\epsilon) << 1$ and that μ_2, μ_1, *and* κ are of

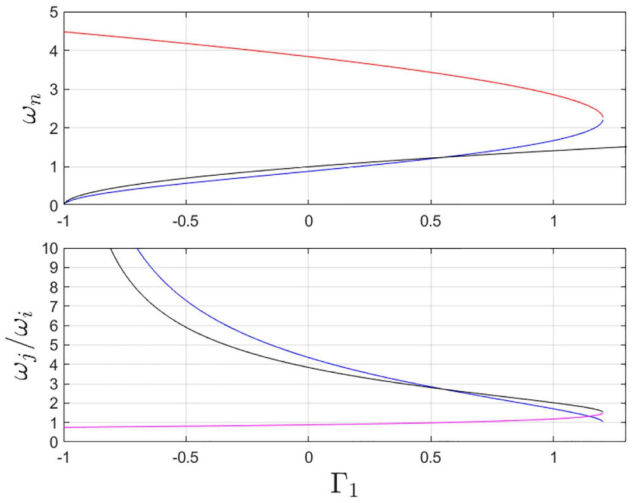

FIG. 3. Natural frequencies $\omega_{4,5}$ (black), ω_6 (blue), and ω_7 (red) with respect to Γ_1 and $\kappa = 1.42$ (top) and their ratios (bottom).

order $O(1)$. This assumption leads to the $O(\epsilon^2)$ ratios

$$\begin{aligned} \epsilon^2 b_1 &= \mu_w/\mu_2, \quad \epsilon^2 b_2 = \mu_3/\mu_2 \\ \epsilon^2 b_3 &= \mu_w/\mu_1, \quad \epsilon^2 b_4 = \mu_3/\mu_1 \end{aligned} \tag{27}$$

and to the $O(1)$ ratios

$$b_5 = 1/\mu_2, \quad b_6 = 1/\mu_1, \quad b_7 = 1/\mu_w. \tag{28}$$

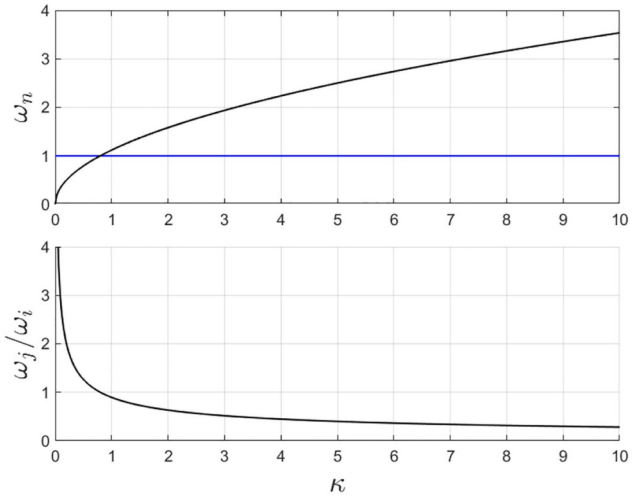

FIG. 4. Natural frequencies ω_1 (black) and ω_2 (blue) of the weakly nonlinear system.

By normalizing the first equation by a factor of μ_2, the second through fourth equations by μ_1, and the fifth through seventh equations by μ_w and substituting Eqs. (27) and (28) into Eq. (26), we obtain

$$\underline{\underline{\mathbf{M}}}\mathbf{q}_{\tau\tau} = \underline{\mathbf{F}}\left(\mathbf{q}, \mathbf{q}_\tau\right), \tag{29}$$

where

$$\underline{\underline{\mathbf{M}}} = \begin{pmatrix} \mu_2 + 3\mu_w & \underline{\underline{\mathbf{m}}}_{12} & \underline{\underline{\mathbf{m}}}_{13} \\ \left(\underline{\underline{\mathbf{m}}}_{12}\right)^T & \mu_1 \cdot \mathbf{I}_{3\times3} & \mu_w \cdot \mathbf{I}_{3\times3} \\ \left(\underline{\underline{\mathbf{m}}}_{13}\right)^T & \mu_w \cdot \mathbf{I}_{3\times3} & \mu_w \cdot \mathbf{I}_{3\times3} \end{pmatrix}$$

and

$$\underline{\mathbf{F}} = \begin{pmatrix} -\epsilon b_2 \sum_{k=i-1}^{i+1} \left[\left(\Delta_k - \frac{\Delta_k^3}{6}\right)\theta_{\tau,k}^2\right] - b_5\kappa\left(\psi - \frac{\psi^3}{6}\right) - b_5\delta_\psi\psi_\tau \\ \epsilon b_4\left(\Delta_{i-1} - \frac{\Delta_{i-1}^3}{6}\right)\psi_\tau^2 - b_6\left(\theta_{i-1} - \frac{\theta_{i-1}^3}{6}\right) - b_6\delta_{\theta,i-1}\theta_{\tau,i-1} \\ \epsilon b_4\left(\Delta_i - \frac{\Delta_i^3}{6}\right)\psi_\tau^2 - b_6\left(\theta_i - \frac{\theta_i^3}{6}\right) - b_6\delta_{\theta,i}\theta_{\tau,i} \\ \epsilon b_4\left(\Delta_{i+1} - \frac{\Delta_{i+1}^3}{6}\right)\psi_\tau^2 - b_6\left(\theta_{i+1} - \frac{\theta_{i+1}^3}{6}\right) - b_6\delta_{\theta,i+1}\theta_{\tau,i+1} \\ b_7\Gamma_3\phi_{\tau,i-1} + b_7\Gamma_2\theta_{\tau,i-1} + b_7\Gamma_1\left(\theta_{i-1} - \frac{\theta_{i-1}^3}{6}\right) \\ b_7\Gamma_3\phi_{\tau,i} + b_7\Gamma_2\theta_{\tau,i} + b_7\Gamma_1\left(\theta_i - \frac{\theta_i^3}{6}\right) \\ b_7\Gamma_3\phi_{\tau,i+1} + b_7\Gamma_2\theta_{\tau,i+1} + b_7\Gamma_1\left(\theta_{i+1} - \frac{\theta_{i+1}^3}{6}\right) \end{pmatrix}.$$

By constructing the bifurcation diagram of the weakly nonlinear cubic order IWP array in Eq. (29) and comparing it to the full weakly nonlinear IWP array in Eq. (10), we find that the Hopf bifurcation is maintained. The bifurcation structure of the cubic order weakly nonlinear system is overlaid on the bifurcation structure of the full weakly nonlinear IWP array (5). The solutions diverge as Γ_3 is increased from the Hopf bifurcation threshold; furthermore, the truncated cubic order system displays only stationary periodic solutions while the full system obtains also non-stationary oscillations and rotations.

B. Order equations

Applying the slow and fast time scales $T_n = \epsilon^n\tau$ and the derivatives with respect to the time scales, we obtain

$$\begin{aligned} \frac{d}{dt} &= \frac{\partial}{\partial T_0}\frac{dT_0}{dt} + \frac{\partial}{\partial T_2}\frac{dT_2}{dt} = D_0 + \epsilon^2 D_2, \\ \frac{d^2}{dt^2} &= \left(D_0 + \epsilon^2 D_2\right)^2 = D_0^2 + 2D_0D_2\epsilon^2 + O\left(\epsilon^4\right). \end{aligned} \tag{30}$$

We assume small angular displacement by expanding the generalized coordinate $\mathbf{q}$ to the approximate solution form

$$\begin{aligned} \mathbf{q} &= \epsilon\begin{bmatrix} q_{11} & q_{21} & \cdots & q_{71} \end{bmatrix}^T + \epsilon^3\begin{bmatrix} q_{13} & q_{23} & \cdots & q_{73} \end{bmatrix}^T \\ &= \epsilon\mathbf{q}_1 + \epsilon^3\mathbf{q}_3. \end{aligned} \tag{31}$$

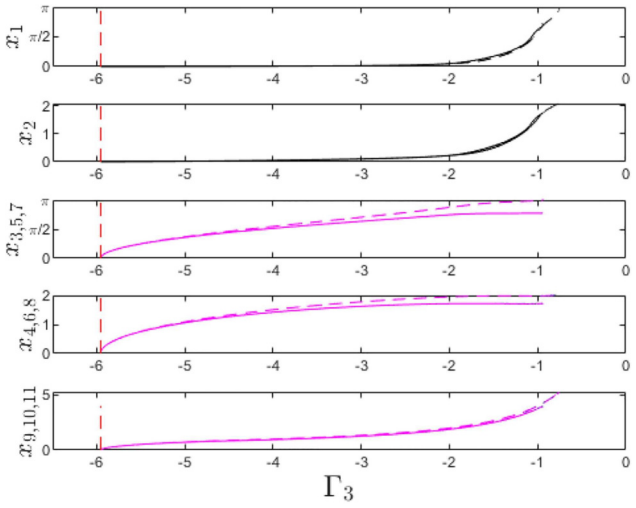

FIG. 5. Bifurcation structure of the weakly nonlinear cubic system (solid) and full system (dashed) for $\Gamma_1 = -4$.

We will assume small gains and small damping to obtain the small parameters,

$$\begin{array}{lll} \Gamma_2 = \epsilon^2\hat{\Gamma}_2 & \Gamma_3 = \epsilon^2\hat{\Gamma}_3 & \delta_\psi = \epsilon^2\hat{\delta}_\psi \\ \delta_{\theta,i-1} = \epsilon^2\hat{\delta}_{\theta,i-1} & \delta_{\theta,i} = \epsilon^2\hat{\delta}_{\theta,i} & \delta_{\theta,i+1} = \epsilon^2\hat{\delta}_{\theta,i+1} \end{array}. \tag{32}$$

By substituting Eqs. (30)–(32) into Eq. (26) and collecting terms of equal order of ϵ, we obtain a set of seven equations. These equations now prove convenient since the first four have trivial solutions, while the last three are dependent on those solutions. By considering the symmetry of the system, we neglect the quadratic terms since the first nonlinear term is cubic.[43] We obtain the order equations,

$O(\epsilon)$:

$$\left[\mathbf{M}_0 D_0^2 + \mathbf{C}_0 D_0 + \mathbf{K}_0\right] \cdot \mathbf{q}_1 = 0, \tag{33}$$

$O(\epsilon^3)$:

$$\left[\mathbf{M}_0 D_0^2 + \mathbf{C}_0 D_0 + \mathbf{K}_0\right] \cdot \mathbf{q}_3 = \left[\mathbf{F}_1 D_2 + \mathbf{F}_2 D_0 - 2 D_0 D_2 \mathbf{M}_0\right] \cdot \mathbf{q}_1 - \mathbf{F}_3 D_0^2 \cdot \mathbf{q}_1 + \frac{1}{6}\mathbf{K}_0 \cdot \mathbf{q}_1^3, \tag{34}$$

where

$$\mathbf{M}_0 = \begin{pmatrix} 1 & 0 & 0 & 0 & 0 & 0 & 0 \\ 0 & 1 & 0 & 0 & 0 & 0 & 0 \\ 0 & 0 & 1 & 0 & 0 & 0 & 0 \\ 0 & 0 & 0 & 1 & 0 & 0 & 0 \\ 1 & 1 & 0 & 0 & 1 & 0 & 0 \\ 1 & 0 & 1 & 0 & 0 & 1 & 0 \\ 1 & 0 & 0 & 1 & 0 & 0 & 1 \end{pmatrix},$$

$$\mathbf{C}_0 = \begin{pmatrix} 0 & 0 & 0 & 0 & 0 & 0 & 0 \\ 0 & 0 & 0 & 0 & 0 & 0 & 0 \\ 0 & 0 & 0 & 0 & 0 & 0 & 0 \\ 0 & 0 & 0 & 0 & 0 & 0 & 0 \\ 0 & 0 & 0 & 0 & -b_7\Gamma_3 & 0 & 0 \\ 0 & 0 & 0 & 0 & 0 & -b_7\Gamma_3 & 0 \\ 0 & 0 & 0 & 0 & 0 & 0 & -b_7\Gamma_3 \end{pmatrix},$$

$$\mathbf{K}_0 = \begin{pmatrix} b_5\kappa & 0 & 0 & 0 & 0 & 0 & 0 \\ 0 & 1 & 0 & 0 & 0 & 0 & 0 \\ 0 & 0 & 1 & 0 & 0 & 0 & 0 \\ 0 & 0 & 0 & 1 & 0 & 0 & 0 \\ 0 & -b_7\Gamma_1 & 0 & 0 & 0 & 0 & 0 \\ 0 & 0 & -b_7\Gamma_1 & 0 & 0 & 0 & 0 \\ 0 & 0 & 0 & -b_7\Gamma_1 & 0 & 0 & 0 \end{pmatrix},$$

$$\mathbf{F}_1 = -\mathbf{C}_0,$$

$$\mathbf{F}_2 = \begin{pmatrix} 3b_1 & b_1+b_2 & b_1+b_2 & b_1+b_2 & b_1 & b_1 & b_1 \\ b_3+b_4 & 0 & 0 & 0 & b_3 & 0 & 0 \\ b_3+b_4 & 0 & 0 & 0 & 0 & b_3 & 0 \\ b_3+b_4 & 0 & 0 & & 0 & 0 & b_3 \\ 0 & 0 & 0 & 0 & 0 & 0 & 0 \\ 0 & 0 & 0 & 0 & 0 & 0 & 0 \\ 0 & 0 & 0 & 0 & 0 & 0 & 0 \end{pmatrix}.$$

C. Solvability condition

The solutions to Eq. (33) can be expressed as

$$\mathbf{q}_1 = \mathbf{v}_1 A_1 e^{i\omega_1 T_0} + \left(\mathbf{v}_2 A_2 + \mathbf{v}_3 A_3 + \mathbf{v}_4 A_4\right) e^{i\omega_2 T_0} + c.c., \tag{35}$$

where $A_i(T_2)$ and its complex conjugate $\bar{A}_i(T_2)$ are yet undetermined complex-valued functions of the slowly varying time scale T_2, and $\mathbf{v_i}$ are the eigenvectors,

$$\begin{aligned} \mathbf{v}_1 &= \begin{pmatrix} 1 & 0 & 0 & 0 & \Lambda_1 & \Lambda_1 & \Lambda_1 \end{pmatrix}^T, \\ \mathbf{v}_2 &= \begin{pmatrix} 0 & 1 & 0 & 0 & \Lambda_2 & 0 & 0 \end{pmatrix}^T, \\ \mathbf{v}_3 &= \begin{pmatrix} 0 & 0 & 1 & 0 & 0 & \Lambda_2 & 0 \end{pmatrix}^T, \\ \mathbf{v}_4 &= \begin{pmatrix} 0 & 0 & 0 & 1 & 0 & 0 & \Lambda_2 \end{pmatrix}^T, \end{aligned} \tag{36}$$

that satisfy the linear system

$$\left[-\omega_n^2 \mathbf{M}_0 + i\omega_n \mathbf{C}_0 + \mathbf{K}_0\right] \cdot \mathbf{v_i} = 0. \tag{37}$$

Furthermore, we quantitatively describe the nearness of ω_1 to ω_2 (4) by introducing the detuning parameter σ defined as

$$\epsilon^2\sigma = \omega_1 - \omega_2. \tag{38}$$

Substituting the solutions: Eqs. (35) and (38) into Eq. (34) yields

$$\left[\mathbf{M}_0 D_0^2 + \mathbf{C}_0 D_0 + \mathbf{K}_0\right] \cdot q_3 = \hat{\mathbf{g}}_1 e^{i\omega_1 T_0} + \hat{\mathbf{g}}_2 e^{-i\omega_1 T_0} + \hat{\mathbf{g}}_3 e^{3i\omega_1 T_0} + \hat{\mathbf{g}}_4 e^{-3i\omega_1 T_0}, \tag{39}$$

where $\hat{\mathbf{g}}_1 = \begin{pmatrix} g_{11} & g_{12} & g_{13} & g_{14} & g_{15} & g_{16} & g_{17} \end{pmatrix}^T$ is the secular term. Vectors $\hat{\mathbf{g}}_i$ are provided explicitly in Appendix H. In order to prevent growth without bound, the secular term must be eliminated, meaning that Eq. (34) has a unique solution if the solvability

condition

$$\mathbf{v}_i^T \cdot \hat{\mathbf{g}}_1 = 0, \quad i = 1 \cdots 4 \tag{40}$$

is satisfied.[42,43] By solving Eq. (40), we now obtain the reduced order system,

$$\begin{bmatrix} g_{11} + \Lambda_1 \left(g_{15} + g_{16} + g_{17}\right) \\ g_{12} + \Lambda_2 g_{15} \\ g_{13} + \Lambda_2 g_{16} \\ g_{14} + \Lambda_2 g_{17} \end{bmatrix} = 0. \tag{41}$$

By substitution and isolation, the evolution equations $D_2 A_i = f_i$ for $i = 1, \ldots, 4$ are obtained from Eq. (41).

D. Slowly varying evolution equations

We express the amplitudes A_i in their polar form $A_i(T_2) = (1/2)\, a_i(T_2)\, e^{i\beta_i(T_2)}$ in the evolution equations. Then by separating real and imaginary parts and rearranging, we obtain the eight slow evolution equations,

$$\begin{aligned} D_2 a_i &= f_{a,i} \\ a_i D_2 \beta_i &= f_{\beta,i} \quad i = 1, \ldots, 4. \end{aligned} \tag{42}$$

Since our goal is to identify the system's synchronized behavior, we use Eq. (42) to eliminate β_i to form the slow flow system phase difference equations. By subtracting the phase equations (*i.e.*, $a_{i+1} D_2 \beta_{i+1} - a_i D_2 \beta_i$), we reduce the set of equations to four amplitude equations and three phase difference equations,

$$\begin{aligned} D_2 a_i &= f_{a,i} \quad i = 1, \ldots, 4, \\ a_1 a_k D_2 \gamma_{jk} &= f_{\gamma,k} \quad k = 2, 3, 4, \end{aligned} \tag{43}$$

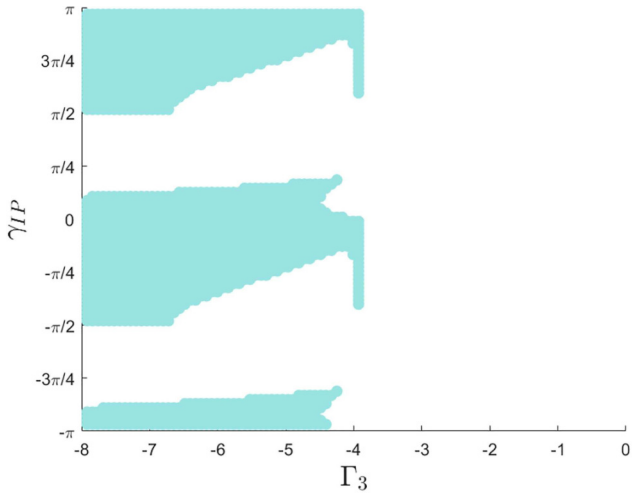

FIG. 6. Stability map of the attainable phase γ_{IP} for IP oscillations as a function of control gain Γ_3.

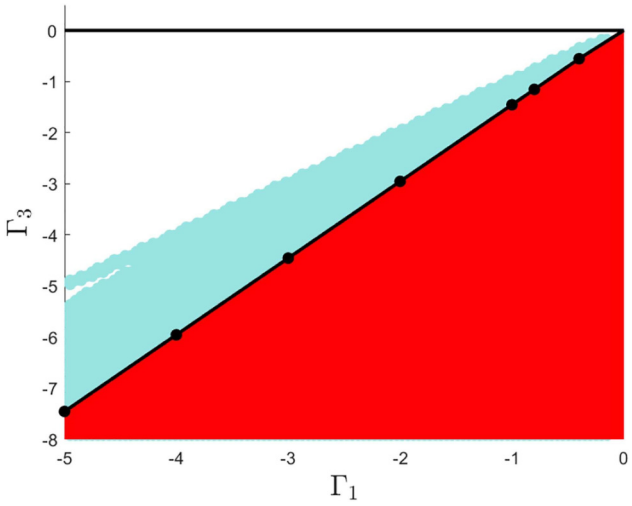

FIG. 7. Stability map of control gains $\Gamma_3(\Gamma_1)$ where the existence of synchronized solutions with constant phase $\gamma_{IP} = -\pi/8$ (blue) appear adjacent to stable equilibrium (red).

where the phase differences γ_{ij} are

$$\begin{aligned} \gamma_{12} &= T_2\sigma + \beta_1 - \beta_2, \\ \gamma_{13} &= T_2\sigma + \beta_1 - \beta_3, \\ \gamma_{14} &= T_2\sigma + \beta_1 - \beta_4. \end{aligned} \tag{44}$$

If all the pendulums are synchronized IP, then any two phase differences $\gamma_{ij} - \gamma_{ik} = 0$. Assuming equal amplitudes of the pendulums, we simplify the notation to $a_1 = A_{1,IP}$ and

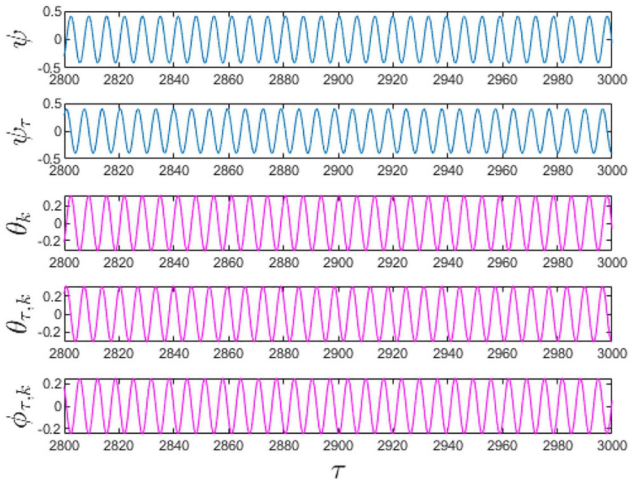

FIG. 8. Time histories of the states for the weakly nonlinear cubic system for control gains $\Gamma_1 = -4$ and $\Gamma_3 = -5$.

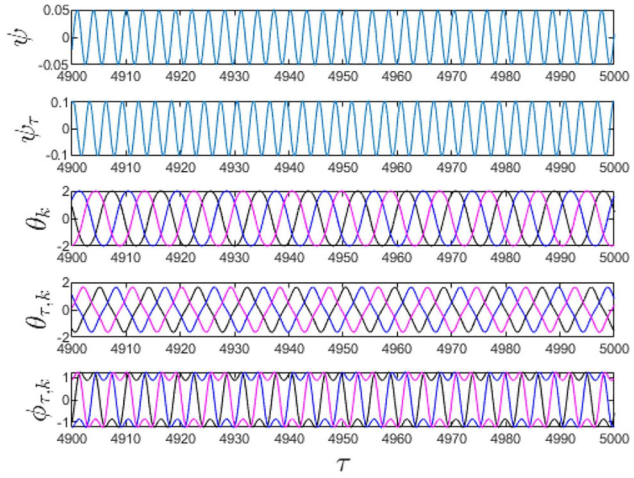

FIG. 9. Time histories of the states for the weakly nonlinear cubic system for control gains $\Gamma_1 = -4$ and $\Gamma_3 = -3$.

$a_2 = a_3 = a_4 = A_{2,IP}$, yielding the synchronized slowly varying evolution equations,

$$D_2 A_{1,IP} = (\eta_1 \sin(\gamma_{IP}) - \eta_2 \cos(\gamma_{IP}))\, A_{2,IP}^3 + (\eta_3 \sin(\gamma_{IP}) - \eta_4 \cos(\gamma_{IP}))\, A_{2,IP} + \eta_5 A_{1,IP} + \eta_6 A_{1,IP}^3,$$

$$D_2 A_{2,IP} = \eta_7 A_{2,IP}^3 + \eta_8 A_{2,IP} + (\eta_9 \sin(\gamma_{IP}) - \eta_{10} \cos(\gamma_{IP}))\, A_{1,IP}^3 + (\eta_{11} \sin(\gamma_{IP}) - \eta_{12} \cos(\gamma_{IP}))\, A_{1,IP}, \quad (45)$$

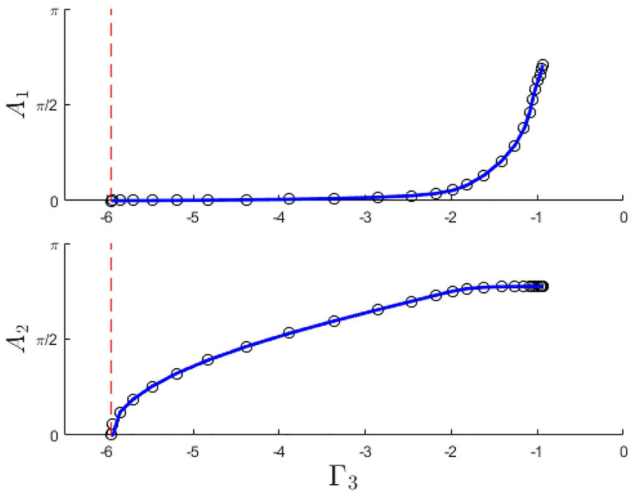

FIG. 10. The bifurcation diagram of the slow flow evolution equations (blue-solid) and the truncated cubic order system (black-circles).

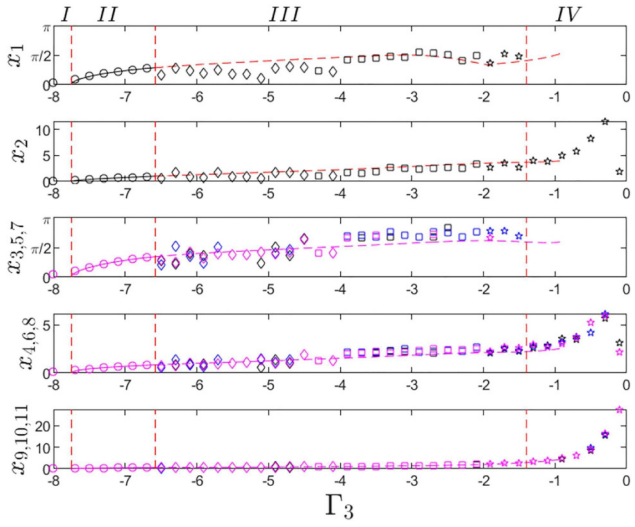

FIG. 11. Bifurcation structure of the strongly nonlinear solution with constant gain Γ_1 where numerical limit cycle amplitudes obtained numerically (circles) are overlaid on values obtained via collocation.

$$A_{1,IP} A_{2,IP} D_2 \gamma_{IP} = \begin{pmatrix} \eta_{13} A_{1,IP}^4 + \eta_{14} A_{1,IP}^2 \\ +\eta_{15} A_{2,IP}^4 + \eta_{16} A_{2,IP}^2 \end{pmatrix} \cos(\gamma_{IP}) + \begin{pmatrix} \eta_{17} A_{1,IP}^4 + \eta_{18} A_{1,IP}^2 \\ +\eta_{19} A_{2,IP}^4 + \eta_{20} A_{2,IP}^2 \end{pmatrix} \sin(\gamma_{IP}) + \left(\eta_{22} A_{2,IP}^3 + \eta_{23} A_{2,IP}\right) A_{1,IP} + \eta_{21} A_{2,IP} A_{1,IP}^3.$$

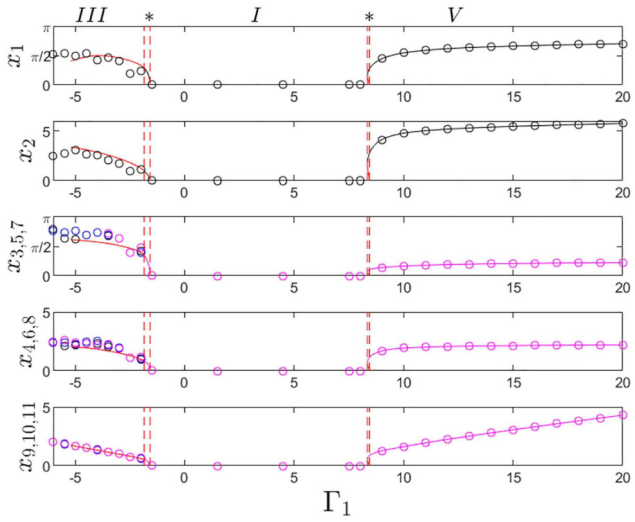

FIG. 12. Bifurcation structure of the strongly nonlinear solution with constant gain Γ_3 where numerical limit cycle amplitudes obtained numerically (circles) are overlaid on values obtained via collocation.

An equilibrium analysis of Eq. (45) yields three equations with two unknown amplitudes $A_{1,IP}$ and $A_{2,IP}$ and an unknown phase of oscillations γ_{IP}. Fixing the phase γ_{IP} and equating the amplitude equations, we obtain the polynomial equation

$$c_9 A_{IP}^9 + c_7 A_{IP}^7 + c_5 A_{IP}^5 + c_3 A_{IP}^3 + c_1 A_{IP} = 0. \tag{46}$$

Since a zero A_{IP} would lead to the stable trivial solution, we can reduce Eq. (46) to the bi-quartic polynomial equation

$$c_9 \left(A_{IP}^2\right)^4 + c_7 \left(A_{IP}^2\right)^3 + c_5 \left(A_{IP}^2\right)^2 + c_2 A_{IP}^2 + c_1 = 0. \tag{47}$$

A non-negativity constraint on the roots of Eq. (47) yields a region in which IP oscillations with respect to phase oscillations, gain Γ_3, and a fixed value of $\Gamma_1 = -4$ are attainable (Fig. 6—cyan region). This yields two regions, the first $\Gamma_3 <\approx -4$ in which bi-stable synchronized and desynchronized solutions exist, and a region $\Gamma_3 >\approx -4$ where no synchronized solutions exist. By fixing the phase of oscillations γ_{IP}, we now find the synchronized solutions with respect to Γ_3 (Γ_1), as displayed in Fig. 7. We note that synchronized solutions exist near the Hopf bifurcation threshold and are lost as Γ_3 grows further from it. An example for the time histories of the states within the region of synchronized solutions reveals stable synchronization (Fig. 8) of the pendula. While, beyond this region, we find the solutions are no longer synchronized (Fig. 9), rather they have a constant phase difference.

The solution to the fixed point analysis of Eq. (45) for a constant gain $\Gamma_1 = -4$ yields a Hopf bifurcation at $\Gamma_3 \approx -6$; overlaying this with the cubic order IWP array given in Eq. (26), we find that a Hopf bifurcation is obtained for matching values and that the error is greatest near the threshold (Fig. 10). Since we did not force a

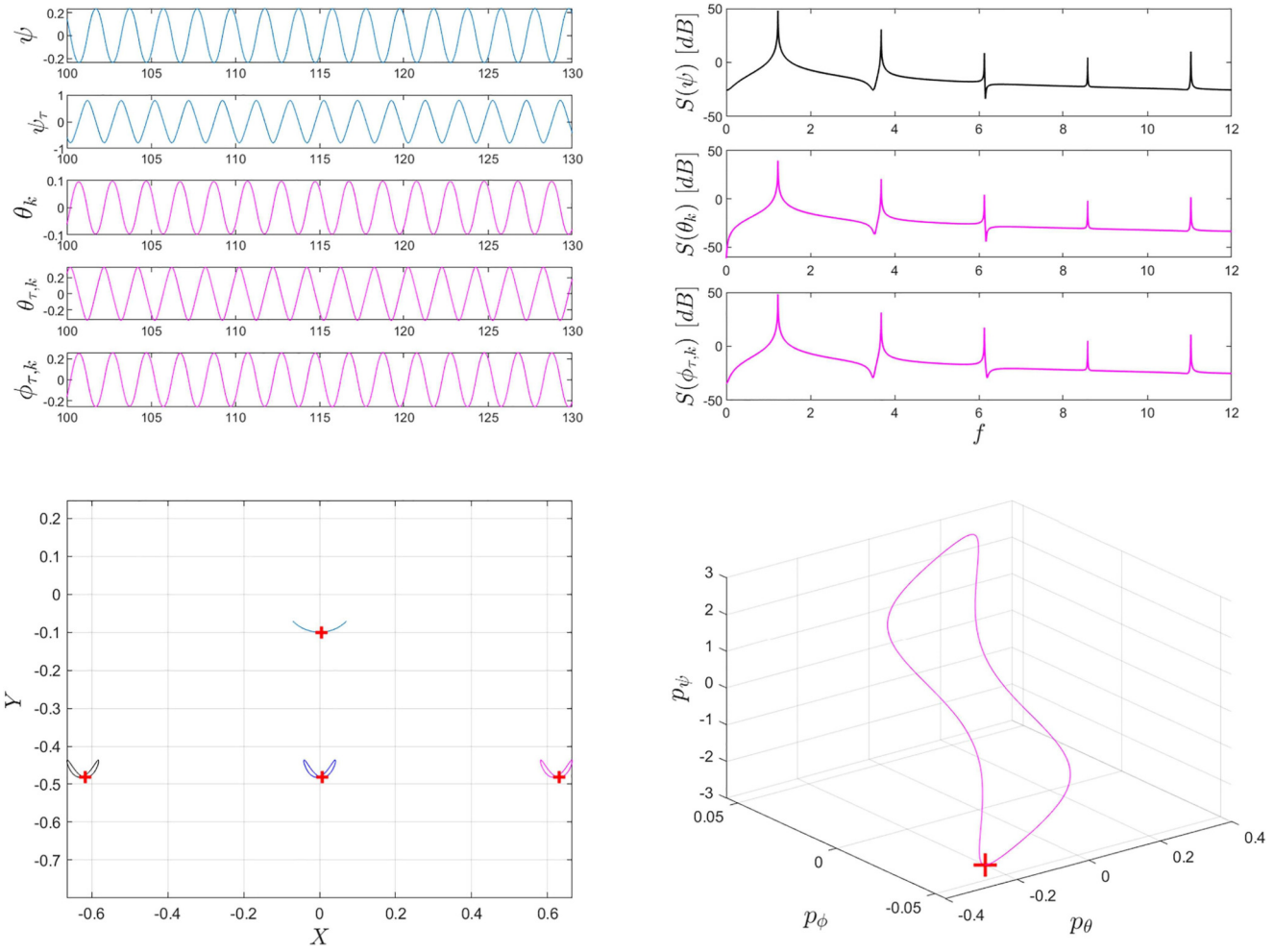

FIG. 13. Time histories of the states (top-left), power spectra (top-right), physical state space and Poincaré map projection (bottom-left), and conjugate momenta Poincaré maps (bottom-right) for $\Gamma_1 = 8.4$ and $\Gamma_3 = -3$. $k = i - 1$(black), $k = i$(blue), and $k = i + 1$(magenta).

detuning of gains Γ_1 and Γ_3 near the Hopf threshold, the bifurcation diagrams are nearly identical as we increase the value of Γ_3 beyond the bifurcation point.

V. NUMERICAL ANALYSIS

A. Bifurcation structure

A numerical bifurcation structure is constructed for the strongly nonlinear IWP array. We note the fixed parameters $\Gamma_2 = 0, \kappa = 1.42$, and initial conditions

$$\mathbf{x_0} = \left(\frac{\pi}{4} \quad 0 \quad \frac{\pi}{4} \quad 0 \quad \frac{\pi}{4} \quad 0 \quad \frac{\pi}{4} \quad \mathbf{0}_{4\times 1}\right)^T. \tag{48}$$

The bifurcation structure is constructed for a sampled range of gains Γ_3 and constant $\Gamma_1 = -4$ (Fig. 11). A Hopf threshold is reached at $\Gamma_3 \approx -7.8$. Three main regions may be identified from Fig. 11. Region I is defined as the region in which $\Gamma_3 < \Gamma_H \approx -7.8$ where the zero equilibrium is stable. The Hopf threshold is reached (dashed

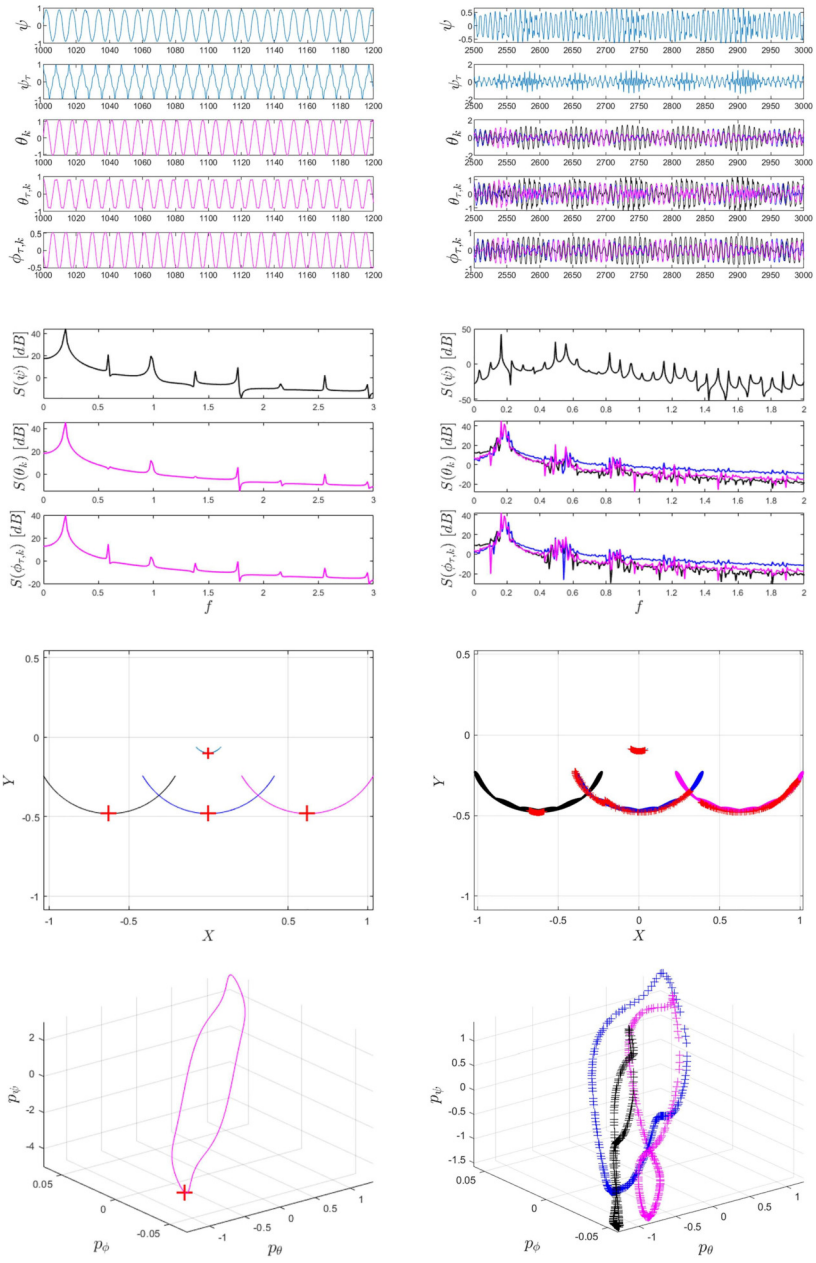

FIG. 14. Time histories of the states (row 1), power spectra (row 2), physical state space and Poincaré map projection (row 3), and conjugate momenta Poincaré maps (row 4) for $\Gamma_3 = -6.6$ and -5 from left to right.

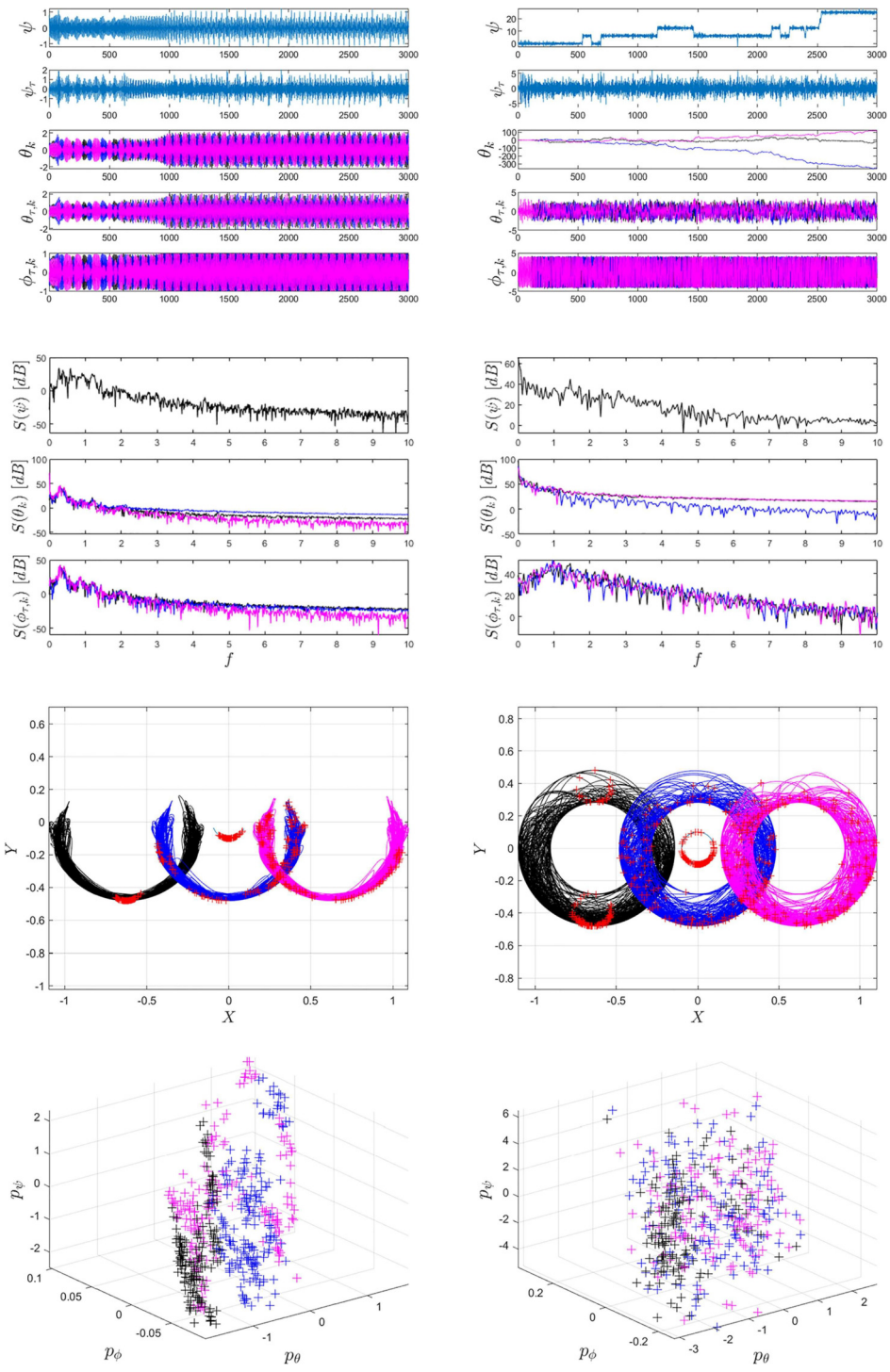

FIG. 15. Time histories of the states (row 1), power spectra (row 2), physical state space and Poincaré map projection (row 3), and conjugate momenta Poincaré maps (row 4) for $\Gamma_3 = -4$ and -1 from left to right.

line) at $\Gamma_3 \approx -7.8$, and the system then enters limit cycle oscillations (region II), the amplitude of oscillations increases as the distance from the Hopf threshold increases. In region III, the rod's amplitude ψ exceeds π, and it now performs rotations and reaches its limit amplitude. We note the limit cycles lose stability when the gain $\Gamma_3 > \Gamma_{3F} \approx -6.58$, where Γ_{3F} is the gain value in which the magnitude of the Floquet multipliers is greater than 1 and a Neimark–Sacker bifurcation is obtained. Furthermore, we plot the bifurcation structure for constant $\Gamma_3 = -3$ and varying values of Γ_1 in Fig. 12. A sub-critical Hopf bifurcation is obtained at $\Gamma_1 \approx 8.4$, and this leads to unstable limit cycles that then reach stability at a limit point cycle. We also obtain a supercritical Hopf bifurcation at $\Gamma_1 \approx -1.6$, and these limit cycles lose stability to a Neimark–Sacker bifurcation at $\Gamma_1 \approx -1.85$. The bifurcation diagrams are constructed by means of two different numerical approaches: (i) by solving the nonlinear differential equations using a Runga–Kutta method (*ODE45*) and (ii) via orthogonal collocation (*MatCont*). The maximum relative error between both methods in region II for an arbitrary state x_5 is $e \approx 0.35$. This maximal error is obtained near the Hopf threshold since the transient there is the longest. In order to analyze the dynamics in each region of the bifurcation structures, numerical simulations were performed. For a time domain analysis, the time histories of the states are plotted along with the physical state space, i.e., the steady-state oscillations of the pendulums and rod in the $Y(X)$ projection and the conjugate momenta projection. The conjugate momenta is defined as $p_i = \partial \mathscr{L} / \partial q_{i,\tau}$, where $\mathbf{q}_\tau = \begin{pmatrix} \psi_\tau & \theta_{k,\tau} & \phi_{k,\tau} \end{pmatrix}$ is the first time derivative of the generalized coordinates. A Poincaré section is then sampled at every positive zero crossing of the wheel angular velocity $\phi_{k,\tau}$ and is then overlaid on the physical state space and the conjugate momenta projection.

B. Periodic and nonstationary oscillations

The IWP array's dynamics are simulated beyond the subcritical Hopf threshold (Fig. 13), and stable periodic solutions are obtained. We show the different solutions obtained by increasing Γ_3 beyond the supercritical Hopf threshold for constant gain $\Gamma_1 = -4$ in Figs. 14 and 15. These numerical simulations reveal stable periodic solutions (Fig. 14 – column 1) for gain values $\Gamma_{3H} < \Gamma_3 < \Gamma_{3F}$ where Γ_{3H} is the value obtained for gain Γ_3 at the Hopf bifurcation point and Γ_{3F} is the value obtained for Γ_3 when the Floquet multipliers lose their stability. For $\Gamma_3 > \Gamma_{3F}$, we obtain quasiperiodic solutions (Fig. 14—column 2), chaotic oscillations (Fig. 15—column 1), and rotations (Fig. 15—column 2).

C. Synchronization and decoherence

The synchronous behavior of the strongly nonlinear system is analyzed by performing a Hilbert transform on the time-dependent signal $x(\tau)$.[15] Since the dynamics of this system can be chaotic, we choose the average phase as the maximal amplitude obtained from the frequency response of the wheel angular velocity. This allows us to construct the analytical signal $x_a(\tau) = x(\tau) + iH[x(\tau)]$ for a narrow-banded signal, which then yields $x_a(\tau) = A(\tau)\, e^{[i\omega\tau + \varphi(\tau)]}$. The phases $\varphi_k(\tau)$ are then used to quantify the synchronization by formulating the Kuramoto order parameter[4]

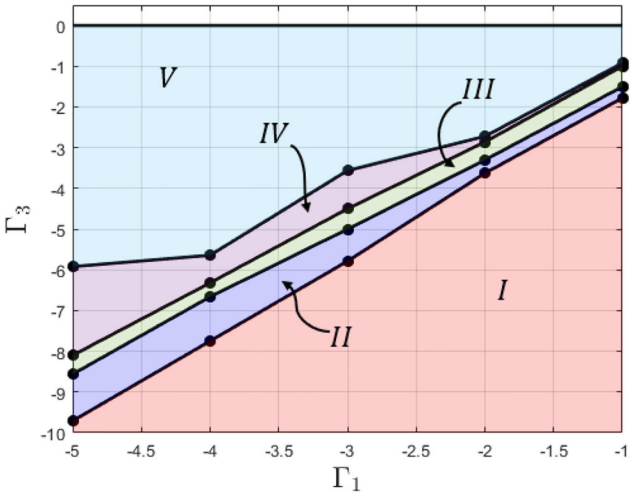

FIG. 16. Stability map of control gains $\Gamma_3(\Gamma_1)$ depicting regions of synchronous decoherent and chimera-like solutions: (*I*) stable equilibrium, (*II*) IP and AP oscillations, (*III*) synchronized and CL states, (*IV*) decoherent and CL states, and (*V*) decoherent states.

$$Z(\tau) = \frac{1}{N} \sum_{k=1}^{N} e^{i\left[\varphi_k(t) - \bar{\varphi}_{\mathrm{syn}}(t)\right]}, \tag{49}$$

where $\bar{\varphi}_{\mathrm{syn}}$ is the average phase of the synchronous population at time τ. A population is then considered to be synchronized if $|Z| \approx 1$ and decoherent when $|Z| \approx 0$. We emphasize that Eq. (49) is directly applicable to phase equations.[44] However, Martens *et al.*[4] demonstrated that considering only the phases of oscillators yields an accurate criterion of transition to chimera states.

A stability map (Fig. 16) is constructed by varying the system's initial conditions. Beyond the region in which the zero equilibrium is stable (region *I*), we find a region with coexisting IP and AP synchronized dynamics (region *II*). This region then transitions into a region in which either all three pendula are synchronized or two of the three are synchronized and the third is desynchronized, we refer to these dynamics as CL (region *III*) in this region coexisting synchronized solutions were also found. The next region consists of CL states together with decoherent solutions (region *IV*). Region *V* is only decoherent. The topology of this map also reveals the ability of the control gains to impact the coupling strength between the oscillators. An example of the synchronous behavior of the single array is given in Fig. 17. It shows gain $\Gamma_3 = -6.6, -5, -4$ from left to right, and the system transitions from an IP synchronized periodic motion to decoherence. The decoherent dynamics are displayed for a quasiperiodic response and for chaotic oscillations and rotations.

D. Chimera-like response

The quasiperiodic response can also enter into a CL state (Fig. 18); in these dynamics, two of the three oscillators are synchronized IP, and the third is asynchronous in relation to them. To

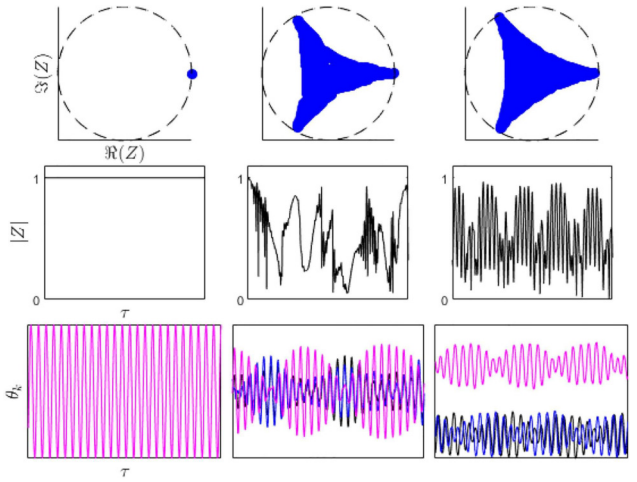

FIG. 17. Oscillator phase (top), Kuramoto parameter $|Z|$ (center), and time histories (bottom) for synchronous to decoherent dynamics with $\Gamma_1 = -4$ and increasing values of Γ_3.

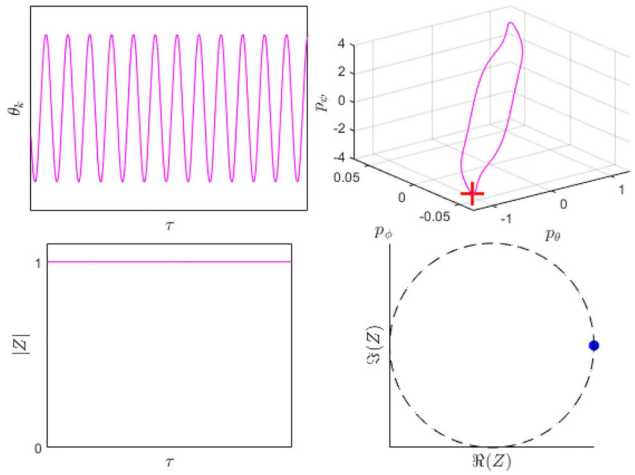

FIG. 19. Time histories (top-left), conjugate momenta Poincaré maps (top-right), the time history of the magnitude of Kuramoto order parameter $|Z|$ (bottom-left), and phase of $|Z|$ for $\Gamma_1 = -4$ and $\Gamma_3 = -6.6$ and IP initial conditions.

illustrate these dynamics, we define two populations within our system: the first is defined as the solution to Eq. (49) for $N = 2$ (noted as $Z_{N=2}$) and the second is for $N = 1$ (noted as $Z_{N=1}$). We use this to display the phases of the populations. However, since the size of Eq. (49) for $N = 1$ is always 1, we display the size of Eq. (49) for $N = 3$ (noted as $Z_{N=3}$). This analysis enables us to define a CL state as a state in which $|Z_{N=3}| \neq 1$, yet the phase of $Z_{N=2} \approx 0$ and $Z_{N=1} \neq 0$.

E. Coexisting solutions

We note that regions *II*, *III*, *and IV* contain different coexisting solutions. We simulate for the initial condition given in Eq. (48) and for $\Gamma_3 = -6.6$ and find a periodic IP synchronized response in Fig. 19. When altering the initial condition to an arbitrary one, we find that a periodic solution is maintained; however, the synchronous dynamics of this solution break down. This solution displays a static pendulum that does not oscillate, while the two remaining display AP synchrony (Fig. 20). This topology and the fact that there are three oscillators cause the size of the Kuramoto order

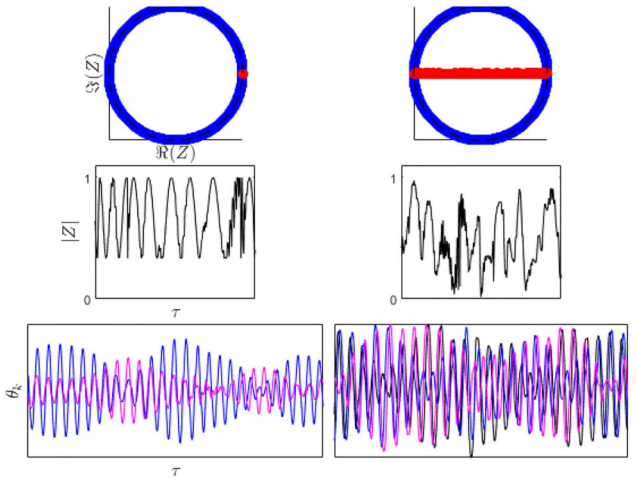

FIG. 18. Oscillator phase (top), Kuramoto parameter $|Z|$ (center), and time histories (bottom) for CL to decoherent dynamics with $\Gamma_1 = -4$ and increasing values of Γ_3.

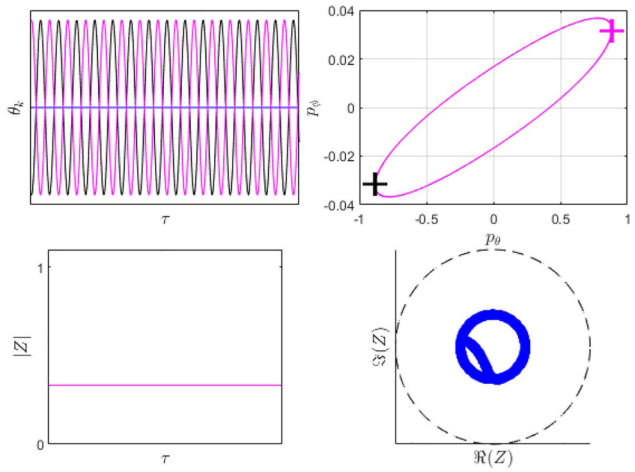

FIG. 20. Time histories (top-left), conjugate momenta Poincaré maps (top-right), the time history of the magnitude of Kuramoto order parameter $|Z|$ (bottom-left), and phase of $|Z|$ for $\Gamma_1 = -4$ and $\Gamma_3 = -6.6$ and arbitrary initial conditions.

parameter to settle at $|Z| \approx 1/3$, this constant value (which is different from $Z = 1$) represents a constant phase difference between the oscillators and is known in the literature as a stable chimera.[45] We note that these coexisting solutions were not uncovered by Martens *et al.*[4]

VI. CLOSING REMARKS

We derive a consistent nonlinear model for the self-excited dynamics of an IWP array that enables the investigation of synchronized, decoherent, and chimera-like states. The dynamical system response includes periodic limit-cycle oscillations and nonstationary quasiperiodic and chaotic dynamics. A weakly nonlinear configuration was derived by tuning the system parameters, and the synchronous nature of the system was analyzed by applying asymptotic multiple scales. This analysis led to algebraic conditions for IP synchronization, revealing a region adjacent to stable equilibrium solutions in which IP synchrony may emerge. The strongly nonlinear dynamics of the IWP array were studied by formulating a bifurcation structure with respect to the linear control law applied to the inertia wheel. This bifurcation structure together with numerical simulations uncovered regions of stable limit cycle oscillations, quasiperiodic solutions, and chaotic oscillations and rotations. A Kuramuto order parameter analysis was applied to investigate the synchronous dynamics of the strongly nonlinear system revealing regions of synchronous and decoherent dynamics. CL states (dynamical states in which two elements are synchronized, whereas the third is desynchronized) were also found by considering a slight alteration to the Kuramoto order analysis. The mapping of these solutions revealed several regions of coexisting solutions, and the progression of solutions from synchronous through a CL state to decoherence when a control gain is increased.

Future research on the synchronous and decoherent dynamics within the IWP array could include experiment-based generalized forces for a more realistic dissipation model for friction in the bearings. Furthermore, the investigation could include alternative nonlinear feedback mechanisms for inertia wheel control to determine the elimination or enlargement of the parameter space of chimera states. We also note some open questions that still remain and could also serve as objectives for future research. Namely, (*i*) is the chimera state a local or global phenomenon? (*ii*) The Kuramoto order parameter Eq. (49) is a very effective tool for determining the degree of synchrony of large arrays of oscillators that are performing periodic oscillations. However, when the size of the array is decreased (as it is in this study), a chimera state is more difficult to uncover. Furthermore, when the oscillators are no longer oscillating with one frequency, but rather are in a state of quasiperiodic or chaotic oscillations, the application of Eq. (49) is far from trivial. Is there another mathematical tool that can be developed to determine the synchrony of non-stationary oscillations?

ACKNOWLEDGMENTS

G.Y. was supported by a Technion graduate studies fellowship. O.G. was partially supported by the Henri Garih Chair in Mechanical Engineering. We thank the reviewers for their constructive comments.

AUTHOR DECLARATIONS

Conflict of Interest

The authors have no conflicts to disclose.

Author Contributions

G. Yakir: Formal analysis (equal); Investigation (equal); Methodology (equal); Validation (equal); Writing – original draft (equal); Writing – review & editing (equal). **O. Gottlieb:** Conceptualization (lead); Formal analysis (equal); Funding acquisition (lead); Investigation (equal); Methodology (equal); Project administration (lead); Supervision (lead); Validation (equal); Writing – original draft (equal); Writing – review & editing (equal).

DATA AVAILABILITY

The data that support the findings of this study are available from the corresponding author upon reasonable request.

APPENDIX A: KINEMATICS

First, we find the distance to the bar and wheel from a fixed point above pendulum i,

$$\begin{aligned}\mathbf{r}_{\psi,1} &= -l_{\psi,x}\hat{x} - l_{\psi,cm}\cos\psi\cdot\hat{y},\\ \mathbf{r}_{\psi,2} &= l_{\psi,x}\hat{x} - l_{\psi,cm}\cos\psi\cdot\hat{y},\\ \mathbf{r}_{\mathbf{b}} &= l_{\psi}\sin\psi\cdot\hat{x} - l_{\psi}\cos\psi\cdot\hat{y}.\end{aligned} \tag{A1}$$

Next, we find the distances to pendulums and wheels $i-1$, i, and $i+1$,

$$\begin{aligned}\mathbf{r}_{\mathbf{p},\mathbf{i-1}} &= (l_\psi\sin\psi + l_p\sin\theta_{i-1} - l_b)\cdot\hat{x} - (l_\psi\cos\psi + l_p\cos\theta_{i-1})\cdot\hat{y},\\ \mathbf{r}_{\mathbf{p},\mathbf{i}} &= (l_\psi\sin\psi + l_p\sin\theta_{i})\cdot\hat{x} - (l_\psi\cos\psi + l_p\cos\theta_{i})\cdot\hat{y},\\ \mathbf{r}_{\mathbf{p},\mathbf{i+1}} &= (l_\psi\sin\psi + l_p\sin\theta_{i+1} + l_b)\cdot\hat{x} - (l_\psi\cos\psi + l_p\cos\theta_{i+1})\cdot\hat{y},\\ \mathbf{r}_{\mathbf{w},\mathbf{i-1}} &= (l_\psi\sin\psi + l_w\sin\theta_{i-1} - l_b)\cdot\hat{x} - (l_\psi\cos\psi + l_w\cos\theta_{i-1})\cdot\hat{y},\\ \mathbf{r}_{\mathbf{w},\mathbf{i}} &= (l_\psi\sin\psi + l_w\sin\theta_{i})\cdot\hat{x} - (l_\psi\cos\psi + l_w\cos\theta_{i})\cdot\hat{y},\\ \mathbf{r}_{\mathbf{w},\mathbf{i+1}} &= (l_\psi\sin\psi + l_w\sin\theta_{i+1} + l_b)\cdot\hat{x} - (l_\psi\cos\psi + l_w\cos\theta_{i+1})\cdot\hat{y}.\end{aligned} \tag{A2}$$

By deriving the distances with respect to time, we find the velocities of the wheel and pendulum,

$$\begin{aligned}\dot{\mathbf{r}}_{p,i-1} &= \left(l_\psi\dot{\psi}\cos\psi + l_p\dot{\theta}_{i-1}\cos\theta_{i-1}\right)\cdot\hat{x}\\ &\quad + \left(l_\psi\dot{\psi}\sin\psi + l_p\dot{\theta}_{i-1}\sin\theta_{i-1}\right)\cdot\hat{y},\end{aligned}$$

$$\dot{\mathbf{r}}_{p,i} = \left(l_\psi\dot{\psi}\cos\psi + l_p\dot{\theta}_{i}\cos\theta_{i}\right)\cdot\hat{x} + \left(l_\psi\dot{\psi}\sin\psi + l_p\dot{\theta}_{i}\sin\theta_{i}\right)\cdot\hat{y},$$

$$\begin{aligned}\dot{\mathbf{r}}_{p,i+1} &= \left(l_\psi\dot{\psi}\cos\psi + l_p\dot{\theta}_{i+1}\cos\theta_{i+1}\right)\cdot\hat{x}\\ &\quad + \left(l_\psi\dot{\psi}\sin\psi + l_p\dot{\theta}_{i+1}\sin\theta_{i+1}\right)\cdot\hat{y},\end{aligned}$$

$$\begin{aligned}\dot{\mathbf{r}}_{w,i-1} &= \left(l_\psi\dot{\psi}\cos\psi + l_w\dot{\theta}_{i-1}\cos\theta_{i-1}\right)\cdot\hat{x}\\ &\quad + \left(l_\psi\dot{\psi}\sin\psi + l_w\dot{\theta}_{i-1}\sin\theta_{i-1}\right)\cdot\hat{y},\end{aligned}$$

$$\dot{\mathbf{r}}_{w,i} = \left(l_\psi \dot{\psi} \cos\psi + l_w \dot{\theta}_i \cos\theta_i\right) \cdot \hat{x} + \left(l_\psi \dot{\psi} \sin\psi + l_w \dot{\theta}_i \sin\theta_i\right) \cdot \hat{y}, \tag{A3}$$

$$\dot{\mathbf{r}}_{w,i+1} = \left(l_\psi \dot{\psi} \cos\psi + l_w \dot{\theta}_{i+1} \cos\theta_{i+1}\right) \cdot \hat{x} + \left(l_\psi \dot{\psi} \sin\psi + l_w \dot{\theta}_{i+1} \sin\theta_{i+1}\right) \cdot \hat{y},$$

$$\mathbf{r}_{\psi,1} = l_{\psi,cm} \dot{\psi} \sin\psi \cdot \hat{y},$$

$$\mathbf{r}_{\psi,2} = l_{\psi,cm} \dot{\psi} \sin\psi \cdot \hat{y},$$

$$\dot{\mathbf{r}}_b = l_\psi \dot{\psi} \cos\psi \cdot \hat{x} + l_\psi \dot{\psi} \sin\psi \cdot \hat{y}.$$

By squaring the velocities, we find

$$\begin{aligned}
\dot{\mathbf{r}}^2_{p,i-1} &= (l_\psi \dot{\psi})^2 + (l_p \dot{\theta}_{i-1})^2 + 2 l_\psi l_p \dot{\psi} \dot{\theta}_{i-1} \cos(\psi - \theta_{i-1}),\\
\dot{\mathbf{r}}^2_{p,i} &= (l_\psi \dot{\psi})^2 + (l_p \dot{\theta}_i)^2 + 2 l_\psi l_p \dot{\psi} \dot{\theta}_i \cos(\psi - \theta_i),\\
\dot{\mathbf{r}}^2_{p,i+1} &= (l_\psi \dot{\psi})^2 + (l_p \dot{\theta}_{i+1})^2 + 2 l_\psi l_p \dot{\psi} \dot{\theta}_{i+1} \cos(\psi - \theta_{i+1}),\\
\dot{\mathbf{r}}^2_{w,i-1} &= (l_\psi \dot{\psi})^2 + (l_w \dot{\theta}_{i-1})^2 + 2 l_\psi l_w \dot{\psi} \dot{\theta}_{i-1} \cos(\psi - \theta_{i-1}),\\
\dot{\mathbf{r}}^2_{w,i} &= (l_\psi \dot{\psi})^2 + (l_w \dot{\theta}_i)^2 + 2 l_\psi l_w \dot{\psi} \dot{\theta}_i \cos(\psi - \theta_i),\\
\dot{\mathbf{r}}^2_{w,i+1} &= (l_\psi \dot{\psi})^2 + (l_w \dot{\theta}_{i+1})^2 + 2 l_\psi l_w \dot{\psi} \dot{\theta}_{i+1} \cos(\psi - \theta_{i+1}),\\
\mathbf{r}^2_{\psi,1} &= (l_{\psi,cm} \dot{\psi} \sin\psi)^2,\\
\mathbf{r}^2_{\psi,2} &= (l_{\psi,cm} \dot{\psi} \sin\psi)^2,\\
\dot{\mathbf{r}}^2_b &= (l_\psi \dot{\psi})^2.
\end{aligned} \tag{A4}$$

APPENDIX B: FORCING VECTOR ELEMENTS

The elements of the generalized forces are given explicitly below:

$$f_1 = \mu_w^3 \det\left(\hat{\mathbf{M}}\right)^{-1} \begin{bmatrix} F_{1567} + F_{52}\mu_3 \cos\Delta_{i-1} \\ + F_{63}\mu_3 \cos\Delta_i + F_{74}\mu_3 \cos\Delta_{i+1} \end{bmatrix},$$

$$f_2 = -\mu_w^3 \det\left(\hat{\mathbf{M}}\right)^{-1} \begin{bmatrix} -F_{52} \begin{pmatrix} \mu_3^2 \cos^2\Delta_i \\ + \mu_3^2 \cos^2\Delta_{i+1} - \mu_2 \end{pmatrix} \\ + \begin{pmatrix} F_{1567} + F_{63}\mu_3 \cos\Delta_i \\ + F_{74}\mu_3 \cos\Delta_{i+1} \end{pmatrix} \mu_3 \cos\Delta_{i-1} \end{bmatrix},$$

$$f_3 = -\mu_w^3 \det\left(\hat{\mathbf{M}}\right)^{-1} \begin{bmatrix} -F_{63} \begin{pmatrix} \mu_3^2 \cos^2\Delta_{i-1} \\ + \mu_3^2 \cos^2\Delta_{i+1} - \mu_2 \end{pmatrix} \\ + \begin{pmatrix} F_{1567} + f_{52}\mu_3 \cos\Delta_{i-1} \\ + F_{74}\mu_3 \cos\Delta_{i+1} \end{pmatrix} \mu_3 \cos\Delta_i \end{bmatrix},$$

$$f_4 = -\mu_w^3 \det\left(\hat{\mathbf{M}}\right)^{-1} \begin{bmatrix} -F_{74} \begin{pmatrix} \mu_3^2 \cos^2\Delta_{i-1} \\ + \mu_3^2 \cos^2\Delta_i \\ - \mu_2 \end{pmatrix} \\ + \begin{pmatrix} F_{1567} \\ + F_{52}\mu_3 \cos\Delta_{i-1} \\ + F_{64}\mu_3 \cos\Delta_i \end{pmatrix} \mu_3 \cos\Delta_{i+1} \end{bmatrix},$$

$$f_5 = -\mu_w^2 \det\left(\hat{\mathbf{M}}\right)^{-1} \begin{bmatrix} F_5 \begin{pmatrix} \mu_3^2 \cos^2\Delta_{i-1} + \mu_3^2 \cos^2\Delta_i \\ + \mu_3^2 \cos^2\Delta_{i+1} - \mu_2 \end{pmatrix} \\ + F_{1567}\mu_w \\ + F_{52}\mu_w \begin{pmatrix} \mu_3^2 \cos^2\Delta_i \\ + \mu_3^2 \cos^2\Delta_{i+1} - \mu_2 \end{pmatrix} \\ - \bar{F}_1 \mu_3 \mu_w \cos\Delta_{i-1} \\ + F_{63}\mu_3\mu_w \cos\Delta_i \\ + F_{74}\mu_3\mu_w \cos\Delta_{i+1} \\ - \begin{pmatrix} F_{63} \cos\Delta_i \\ + F_{74} \cos\Delta_{i+1} \end{pmatrix} \mu_3^2 \mu_w \cos\Delta_{i-1} \end{bmatrix},$$

$$f_6 = -\mu_w^2 \det\left(\hat{\mathbf{M}}\right)^{-1} \begin{bmatrix} F_6 \begin{pmatrix} \mu_3^2 \cos^2\Delta_{i-1} + \mu_3^2 \cos^2\Delta_i \\ + \mu_3^2 \cos^2\Delta_{i+1} - \mu_2 \end{pmatrix} \\ + F_{1567}\mu_w \\ + F_{63}\mu_w \begin{pmatrix} \mu_3^2 \cos^2\Delta_{i-1} \\ + \mu_3^2 \cos^2\Delta_{i+1} - \mu_2 \end{pmatrix} \\ - \bar{F}_2 \mu_3 \mu_w \cos\Delta_i \\ + F_{52}\mu_3\mu_w \cos\Delta_{i-1} \\ + F_{74}\mu_3\mu_w \cos\Delta_{i+1} \\ - \begin{pmatrix} F_{52} \cos\Delta_{i-1} \\ + F_{74} \cos\Delta_{i+1} \end{pmatrix} \mu_3^2 \mu_w \cos\Delta_i \end{bmatrix},$$

$$f_7 = -\mu_w^2 \det\left(\hat{\mathbf{M}}\right)^{-1} \begin{bmatrix} F_7 \begin{pmatrix} \mu_3^2 \cos^2\Delta_{i-1} + \mu_3^2 \cos^2\Delta_i \\ + \mu_3^2 \cos^2\Delta_{i+1} - \mu_2 \end{pmatrix} \\ + F_{1567}\mu_w \\ + F_{74}\mu_w \begin{pmatrix} \mu_3^2 \cos^2\Delta_{i-1} \\ + \mu_3^2 \cos^2\Delta_{i+1} - \mu_2 \end{pmatrix} \\ - \bar{F}_3 \mu_3 \mu_w \cos\Delta_{i+1} \\ + F_{52}\mu_3\mu_w \cos\Delta_{i-1} \\ + F_{63}\mu_3\mu_w \cos\Delta_i \\ - \begin{pmatrix} F_{52} \cos\Delta_{i-1} \\ + F_{63} \cos\Delta_i \end{pmatrix} \mu_3^2 \mu_w \cos\Delta_{i+1} \end{bmatrix},$$

and

$$\det\left(\hat{\mathbf{M}}\right) = -\mu_w^3 \left(\mu_3^2 \cos^2\Delta_{i-1} + \mu_3^2 \cos^2\Delta_i + \mu_3^2 \cos^2\Delta_{i+1} - \mu_2\right),$$

$$\begin{aligned}
F_{1567} &= F_1 - F_5 - F_6 - F_7,\\
F_{52} &= F_5 - F_2,\\
F_{63} &= F_6 - F_3,\\
F_{74} &= F_7 - F_4,\\
\bar{F}_1 &= F_1 + F_2 - 2F_5 - F_6 - F_7,\\
\bar{F}_2 &= F_1 + F_3 - F_5 - 2F_6 - F_7,\\
\bar{F}_3 &= F_1 + F_4 - F_5 - F_6 - 2F_7.
\end{aligned} \tag{B1}$$

APPENDIX C: DIMENSIONAL PARAMETERS

The dimensional parameters as estimated from previous experimental setups[37,38] are given in Table III.

TABLE III. Dimensions of system elements in SI units.

Rod	Beam	Pendulum	Wheel
$l_\psi = 0.1$	$l_b = 1.246$	$l_H = 0.382$	$l_w = 0.2865$
$w_\psi = 0.02$	$w_b = 0.02$	$w_p = 0.02$	$d_w = 0.3735$
$t_\psi = 0.01$	$t_b = 0.01$	$t_p = 0.01$	$t_w = 0.02$
$m_\psi = 0.054$	$m_b = 0.6728$	$m_p = 0.2063$	$m_w = 5.9165$
$I_\psi = 4.68 \times 10^{-5}$	$I_b = 0.0871$	$I_p = 0.0025$	$I_w = 0.0026$
$l_{\psi,cm} = 0.05$		$l_p = 0.191$	

APPENDIX D: MatCont FREE PARAMETERS

The free parameters used in all *MatCont* schemes are as follows:

TABLE IV. Free parameters used in *MatCont*.

InitStepSize	1×10^{-4}
MinStepSize	1×10^{-10}
MaxStepSize	1×10^{-2}
MaxNewtonIters	3
MaxCorrIters	10
MaxTestIters	10
VarTolerance	1×10^{-10}
FunTolerance	1×10^{-10}
TestTolerance	1×10^{-10}
Adapt	5
Jacobian Increment	1×10^{-10}

APPENDIX E: ANALYTICAL HOPF THRESHOLD ($x \in \mathbb{R}^{11}$)

Following Guckenheimer *et al.*,[41] we construct the Jacobian matrix $\mathbf{J}$, and the characteristic polynomial $\sum_{n=0}^{11} c_n \lambda^n$. We define the Sylvester matrix of the system as

$$\mathbf{S} = \begin{pmatrix} c_0 & c_2 & c_4 & c_6 & c_8 & c_{10} & 0 & 0 & 0 & 0 \\ 0 & c_0 & c_2 & c_4 & c_6 & c_8 & c_{10} & 0 & 0 & 0 \\ 0 & 0 & c_0 & c_2 & c_4 & c_6 & c_8 & c_{10} & 0 & 0 \\ 0 & 0 & 0 & c_0 & c_2 & c_4 & c_6 & c_8 & c_{10} & 0 \\ 0 & 0 & 0 & 0 & c_0 & c_2 & c_4 & c_6 & c_8 & c_{10} \\ c_1 & c_3 & c_5 & c_7 & c_9 & 1 & 0 & 0 & 0 & 0 \\ 0 & c_1 & c_3 & c_5 & c_7 & c_9 & 1 & 0 & 0 & 0 \\ 0 & 0 & c_1 & c_3 & c_5 & c_7 & c_9 & 1 & 0 & 0 \\ 0 & 0 & 0 & c_1 & c_3 & c_5 & c_7 & c_9 & 1 & 0 \\ 0 & 0 & 0 & 0 & c_1 & c_3 & c_5 & c_7 & c_9 & 1 \end{pmatrix}, \tag{E1}$$

and the sub-matrices $\mathbf{S_0}$ and $\mathbf{S_1}$ are

$$\mathbf{S_0} = \begin{pmatrix} c_2 & c_4 & c_6 & c_8 & c_{10} & 0 & 0 & 0 \\ c_0 & c_2 & c_4 & c_6 & c_8 & c_{10} & 0 & 0 \\ 0 & c_0 & c_2 & c_4 & c_6 & c_8 & c_{10} & 0 \\ c_5 & c_7 & c_9 & 1 & 0 & 0 & 0 & 0 \\ c_3 & c_5 & c_7 & c_9 & 1 & 0 & 0 & 0 \\ c_1 & c_3 & c_5 & c_7 & c_9 & 1 & 0 & 0 \\ 0 & c_1 & c_3 & c_5 & c_7 & c_9 & 1 & 0 \\ 0 & 0 & c_1 & c_3 & c_5 & c_7 & c_9 & 1 \end{pmatrix},$$

$$\mathbf{S_1} = \begin{pmatrix} c_0 & c_4 & c_6 & c_8 & c_{10} & 0 & 0 & 0 \\ 0 & c_2 & c_4 & c_6 & c_8 & c_{10} & 0 & 0 \\ 0 & c_0 & c_2 & c_4 & c_6 & c_8 & c_{10} & 0 \\ c_3 & c_7 & c_9 & 1 & 0 & 0 & 0 & 0 \\ c_1 & c_5 & c_7 & c_9 & 1 & 0 & 0 & 0 \\ 0 & c_3 & c_5 & c_7 & c_9 & 1 & 0 & 0 \\ 0 & c_1 & c_3 & c_5 & c_7 & c_9 & 1 & 0 \\ 0 & 0 & c_1 & c_3 & c_5 & c_7 & c_9 & 1 \end{pmatrix}. \tag{E2}$$

The solution satisfying

$$\det \mathbf{S} = 0 \quad \text{and} \quad \det \mathbf{S_0} \cdot \det \mathbf{S_1} > 0 \tag{E3}$$

produces one pair of pure imaginary eigenvalues for the Jacobian matrix $\mathbf{J}$ of the single array system.

APPENDIX F: COEFFICIENTS OF NATURAL FREQUENCIES

$$\begin{aligned} a_5 = \Bigg\{ & \Gamma_1^2(\mu_2 - \mu_3 \cos\Delta_{i-1})^2 + 2\Gamma_1^2(\cos\Delta_i + \cos\Delta_{i+1}) \Bigg[(\mu_3 - \mu_2) \\ & + \frac{1}{2}(\cos\Delta_i + \cos\Delta_{i+1}) - 2\Gamma_1\kappa\mu_2 \\ & + 4\Gamma_1\kappa\mu_3^2 \sum_{k=i-1}^{i+1} (\cos^2\Delta_k) - 2\Gamma_1\kappa\mu_3 \sum_{k=i-1}^{i+1} (\cos\Delta_k) \\ & + 2\Gamma_1\mu_2 \left(\mu_2 - \mu_3 \sum_{k=i-1}^{i+1} (\cos\Delta_k) \right) \\ & + 4\kappa\mu_3^2 \sum_{k=i-1}^{i+1} (\cos^2\Delta_k) + (\kappa - \mu_2)^2 \Bigg] \Bigg\}^{1/2}, \end{aligned} \tag{F1}$$

$$a_6 = \Bigg\{ \Gamma_1^2 \left[(\mu_2 - \mu_3 \sum_{k=i-1}^{i+1} (\cos\Delta_k) \right]^2 - 2\Gamma_1\kappa \left[\mu_2 - 2\mu_3^2 \sum_{k=i-1}^{i+1} \left(\cos^2\Delta_k\right) + \mu_3 \sum_{k=i-1}^{i+1} (\cos\Delta_k) \right] + 2\Gamma_1\mu_2 \left[\mu_2 - \Gamma_1\mu_3 \sum_{k=i-1}^{i+1} (\cos\Delta_k) \right] + 4\kappa\mu_3^2 \sum_{k=i-1}^{i+1} \left(\cos^2\Delta_k\right) + (\kappa - \mu_2)^2 \Bigg\}^{1/2}. \tag{F2}$$

APPENDIX G: CUBIC ORDER SYSTEM

$$\hat{\mathbf{M}} = \begin{pmatrix} \mu_2 + 3\mu_w & \underline{\mathbf{m}}_{\mathbf{12}} & \underline{\mathbf{m}}_{\mathbf{13}} \\ (\underline{\mathbf{m}}_{\mathbf{12}})^T & \mu_1 \cdot \mathbf{I}_{3\times 3} & \mu_w \cdot \mathbf{I}_{3\times 3} \\ (\underline{\mathbf{m}}_{\mathbf{13}})^T & \mu_w \cdot \mathbf{I}_{3\times 3} & \mu_w \cdot \mathbf{I}_{3\times 3} \end{pmatrix},$$

$$\underline{\mathbf{F}} = \begin{pmatrix} -\mu_3 \sum_{k=i-1}^{i+1} \left[\left(\Delta_k - \frac{\Delta_k^3}{6} \right) \theta_{\tau,k}^2 \right] - K \left(\psi - \frac{\psi^3}{6} \right) - \delta_\psi \psi_\tau \\ \mu_3 \left(\Delta_{i-1} - \frac{\Delta_{i-1}^3}{6} \right) \psi_\tau^2 - \left(\theta_{i-1} - \frac{\theta_{i-1}^3}{6} \right) - \delta_{\theta,i-1}\theta_{\tau,i-1} \\ \mu_3 \left(\Delta_i - \frac{\Delta_i^3}{6} \right) \psi_\tau^2 - \left(\theta_i - \frac{\theta_i^3}{6} \right) - \delta_{\theta,i}\theta_{\tau,i} \\ \mu_3 \left(\Delta_{i+1} - \frac{\Delta_{i+1}^3}{6} \right) \psi_\tau^2 - \left(\theta_{i+1} - \frac{\theta_{i+1}^3}{6} \right) - \delta_{\theta,i+1}\theta_{\tau,i+1} \\ \Gamma_3\phi_{\tau,i-1} + \Gamma_2\theta_{\tau,i-1} + \Gamma_1 \left(\theta_{i-1} - \frac{\theta_{i-1}^3}{6} \right) \\ \Gamma_3\phi_{\tau,i} + \Gamma_2\theta_{\tau,i} + \Gamma_1 \left(\theta_i - \frac{\theta_i^3}{6} \right) \\ \Gamma_3\phi_{\tau,i+1} + \Gamma_2\theta_{\tau,i+1} + \Gamma_1 \left(\theta_{i+1} - \frac{\theta_{i+1}^3}{6} \right) \end{pmatrix}.$$

APPENDIX H: SECULAR TERMS

$$g_{11} = (-2\,\omega_2\,\mathrm{i})\,\mathrm{e}^{T_2\,\sigma\,\mathrm{i}}\,\frac{\partial}{\partial T_2}\,A_1 + \frac{\kappa\,b_5}{2}\,\mathrm{e}^{T_2\,\sigma\,\mathrm{i}}\,\bar{A}_1 {A_1}^2 + \left(3\,b_1\,{\omega_2}^2 - b_5\,\delta_\psi\,\omega_2\,\mathrm{i} - \frac{3\,b_1\,{\omega_2}^3}{\omega_2 + \Gamma_3\,b_7\,\mathrm{i}}\right)\mathrm{e}^{T_2\,\sigma\,\mathrm{i}}\,A_1 + \left({b_1\,{\omega_2}^2} + b_2\,{\omega_2}^2 - \frac{b_1\,{\omega_2}^3}{\omega_2 + \Gamma_3\,b_7\,\mathrm{i}} - \frac{\Gamma_1\,b_1\,b_7\,\omega_2}{\omega_2 + \Gamma_3\,b_7\,\mathrm{i}}\right)A_2 + \left({b_1\,{\omega_2}^2} + b_2\,{\omega_2}^2 - \frac{b_1\,{\omega_2}^3}{\omega_2 + \Gamma_3\,b_7\,\mathrm{i}} - \frac{\Gamma_1\,b_1\,b_7\,\omega_2}{\omega_2 + \Gamma_3\,b_7\,\mathrm{i}}\right)A_3 + \left({b_1\,{\omega_2}^2} + b_2\,{\omega_2}^2 - \frac{b_1\,{\omega_2}^3}{\omega_2 + \Gamma_3\,b_7\,\mathrm{i}} - \frac{\Gamma_1\,b_1\,b_7\,\omega_2}{\omega_2 + \Gamma_3\,b_7\,\mathrm{i}}\right)A_4, \tag{H1}$$

$$g_{12} = (-2\,\omega_2\,\mathrm{i})\,\frac{\partial}{\partial T_2}\,A_2 + \frac{1}{2}\,\bar{A}_2\,{A_2}^2 + \left(b_3\,{\omega_2}^2 + b_4\,{\omega_2}^2 - \frac{b_3\,{\omega_2}^3}{\omega_2 + \Gamma_3\,b_7\,\mathrm{i}}\right)\mathrm{e}^{T_2\,\sigma\,\mathrm{i}}\,A_1 + \left(-b_6\,\delta_{\theta,i-1}\,\omega_2\,\mathrm{i} - \frac{b_3\,{\omega_2}^3}{\omega_2 + \Gamma_3\,b_7\,\mathrm{i}} - \frac{\Gamma_1\,b_3\,b_7\,\omega_2}{\omega_2 + \Gamma_3\,b_7\,\mathrm{i}}\right)A_2, \tag{H2}$$

$$g_{13} = (-2\,\omega_2\,\mathrm{i})\,\frac{\partial}{\partial T_2}\,A_3 + \frac{1}{2}\,\bar{A}_3\,{A_3}^2 + \left(b_3\,{\omega_2}^2 + b_4\,{\omega_2}^2 - \frac{b_3\,{\omega_2}^3}{\omega_2 + \Gamma_3\,b_7\,\mathrm{i}}\right)\mathrm{e}^{T_2\,\sigma\,\mathrm{i}}\,A_1 + \left(-b_6\,\delta_{\theta,i}\,\omega_2\,\mathrm{i} - \frac{b_3\,{\omega_2}^3}{\omega_2 + \Gamma_3\,b_7\,\mathrm{i}} - \frac{\Gamma_1\,b_3\,b_7\,\omega_2}{\omega_2 + \Gamma_3\,b_7\,\mathrm{i}}\right)A_3, \tag{H3}$$

$$g_{14} = (-2\,\omega_2\,\mathrm{i})\,\frac{\partial}{\partial T_2}\,A_4 + \frac{1}{2}\,\bar{A}_4\,{A_4}^2 + \left(b_3\,{\omega_2}^2 + b_4\,{\omega_2}^2 - \frac{b_3\,{\omega_2}^3}{\omega_2 + \Gamma_3\,b_7\,\mathrm{i}}\right)\mathrm{e}^{T_2\,\sigma\,\mathrm{i}}\,A_1 + \left(-b_6\,\delta_{\theta,i+1}\,\omega_2\,\mathrm{i} - \frac{b_3\,{\omega_2}^3}{\omega_2 + \Gamma_3\,b_7\,\mathrm{i}} - \frac{\Gamma_1\,b_3\,b_7\,\omega_2}{\omega_2 + \Gamma_3\,b_7\,\mathrm{i}}\right)A_4, \tag{H4}$$

$$g_{15} = \left(-\frac{2\,\Gamma_3\,b_7\,{\omega_2}^2\left(\Gamma_3\,b_7 + \omega_2\,\mathrm{i}\right)\mathrm{i}}{2\,{\Gamma_3}^2\,{b_7}^2\,\omega_2 + 2\,{\omega_2}^3}\right)\mathrm{e}^{T_2\,\sigma\,\mathrm{i}}\,\frac{\partial}{\partial T_2}\,A_1 + \frac{b_7\left(\Gamma_3\,b_7 + \omega_2\,\mathrm{i}\right)\left(-2\,\mathrm{i}\,\Gamma_3\,{\omega_2}^2 + 4\,\Gamma_1\,\omega_2 + 2\,\Gamma_1\,\Gamma_3\,b_7\,\mathrm{i}\right)}{2\,{\Gamma_3}^2\,{b_7}^2\,\omega_2 + 2\,{\omega_2}^3} \times \frac{\partial}{\partial T_2}\,A_2 + \frac{b_7\left(\Gamma_3\,b_7 + \omega_2\,\mathrm{i}\right)\left(2\,\Gamma_2\,{\omega_2}^3 + 2\,\mathrm{i}\,\Gamma_2\,\Gamma_3\,b_7\,{\omega_2}^2\right)}{2\,{\Gamma_3}^2\,{b_7}^2\,\omega_2 + 2\,{\omega_2}^3}\,A_2 + \frac{b_7\left(\Gamma_3\,b_7 + \omega_2\,\mathrm{i}\right)\left(-\Gamma_1\,\Gamma_3\,b_7\,\omega_2 + \Gamma_1\,{\omega_2}^2\,\mathrm{i}\right)}{2\,{\Gamma_3}^2\,{b_7}^2\,\omega_2 + 2\,{\omega_2}^3}\,\bar{A}_2\,{A_2}^2, \tag{H5}$$

$$g_{16} = \left(-\frac{2\,\Gamma_3\,b_7\,{\omega_2}^2\left(\Gamma_3\,b_7 + \omega_2\,\mathrm{i}\right)\mathrm{i}}{2\,{\Gamma_3}^2\,{b_7}^2\,\omega_2 + 2\,{\omega_2}^3}\right)\mathrm{e}^{T_2\,\sigma\,\mathrm{i}}\,\frac{\partial}{\partial T_2}\,A_1 + \frac{b_7\left(\Gamma_3\,b_7 + \omega_2\,\mathrm{i}\right)\left(-2\,\mathrm{i}\,\Gamma_3\,{\omega_2}^2 + 4\,\Gamma_1\,\omega_2 + 2\,\Gamma_1\,\Gamma_3\,b_7\,\mathrm{i}\right)}{2\,{\Gamma_3}^2\,{b_7}^2\,\omega_2 + 2\,{\omega_2}^3} \times \frac{\partial}{\partial T_2}\,A_3 + \frac{b_7\left(\Gamma_3\,b_7 + \omega_2\,\mathrm{i}\right)\left(2\,\Gamma_2\,{\omega_2}^3 + 2\,\mathrm{i}\,\Gamma_2\,\Gamma_3\,b_7\,{\omega_2}^2\right)}{2\,{\Gamma_3}^2\,{b_7}^2\,\omega_2 + 2\,{\omega_2}^3}\,A_3 + \frac{b_7\left(\Gamma_3\,b_7 + \omega_2\,\mathrm{i}\right)\left(-\Gamma_1\,\Gamma_3\,b_7\,\omega_2 + \Gamma_1\,{\omega_2}^2\,\mathrm{i}\right)}{2\,{\Gamma_3}^2\,{b_7}^2\,\omega_2 + 2\,{\omega_2}^3}\,\bar{A}_3\,{A_3}^2, \tag{H6}$$

$$g_{17} = \left(-\frac{2\,\Gamma_3\,b_7\,{\omega_2}^2\left(\Gamma_3\,b_7+\omega_2\,\mathrm{i}\right)\mathrm{i}}{2\,{\Gamma_3}^2\,{b_7}^2\,\omega_2+2\,{\omega_2}^3} \right) \mathrm{e}^{T_2\,\sigma\,\mathrm{i}}\,\frac{\partial}{\partial T_2}\,A_1 + \frac{b_7\left(\Gamma_3\,b_7+\omega_2\,\mathrm{i}\right)\left(-2\,\mathrm{i}\,\Gamma_3\,{\omega_2}^2+4\,\Gamma_1\,\omega_2+2\,\Gamma_1\,\Gamma_3\,b_7\,\mathrm{i}\right)}{2\,{\Gamma_3}^2\,{b_7}^2\,\omega_2+2\,{\omega_2}^3} \times \frac{\partial}{\partial T_2}\,A_4 + \frac{b_7\left(\Gamma_3\,b_7+\omega_2\,\mathrm{i}\right)\left(2\,\Gamma_2\,{\omega_2}^3+2\,\mathrm{i}\,\Gamma_2\,\Gamma_3\,b_7\,{\omega_2}^2\right)}{2\,{\Gamma_3}^2\,{b_7}^2\,\omega_2+2\,{\omega_2}^3}\,A_4 + \frac{b_7\left(\Gamma_3\,b_7+\omega_2\,\mathrm{i}\right)\left(-\Gamma_1\,\Gamma_3\,b_7\,\omega_2+\Gamma_1\,{\omega_2}^2\,\mathrm{i}\right)}{2\,{\Gamma_3}^2\,{b_7}^2\,\omega_2+2\,{\omega_2}^3}\,\bar{A}_4\,{A_4}^2. \quad \text{(H7)}$$

REFERENCES

[1] H. Ulrichs, A. Mann, and U. Parlitz, "Synchronization and chaotic dynamics of coupled mechanical metronomes," Chaos **19**, 043120 (2009).
[2] P. Koluda, P. Brzeski, and P. Perlikowski, "Dynamics of n coupled double pendula suspended to the moving beam," Int. J. Struct. Stab. Dyn. **14**, 1440028 (2014).
[3] P. Kambali, F. Torres, N. Barniol, and O. Gottlieb, "Nonlinear multi-element interactions in an elastically coupled microcantilever array subject to electrodynamic excitation," Nonlinear Dyn. **98**, 3067–3094 (2019).
[4] E. A. Martens, S. Thutupalli, A. Fourrière, and O. Hallatschek, "Chimera states in mechanical oscillator networks," Proc. Natl. Acad. Sci. U.S.A. **110**, 10563–10567 (2013).
[5] G. H. Goldsztein, A. N. Nadeau, and S. H. Strogatz, "Synchronization of clocks and metronomes: A perturbation analysis based on multiple timescales," Chaos **31**, 023109 (2021).
[6] D. Block, K. Åström, and M. Spong, *The Reaction Wheel Pendulum*, Synthesis Lectures on Control and Mechatronics (Morgan & Claypool, Princeton, 2007).
[7] M. W. Spong, P. Corke, and R. Lozano, "Nonlinear control of the reaction wheel pendulum," Automatica **37**, 1845–1851 (2001).
[8] H. Gritli and S. Belghith, "Robust feedback control of the underactuated inertia wheel inverted pendulum under parametric uncertainties and subject to external disturbances: LMI formulation," J. Franklin Inst. **355**, 9150–9191 (2018), Special Issue on Control and Signal Processing in Mechatronic Systems.
[9] J. Biswas and B. Seth, "Dynamic stabilisation of a reaction-wheel actuated wheel-robot," Int. J. Factory Autom. Rob. Soft Comput. **4**, 96–101 (2008).
[10] K. J. Åström and K. Furuta, "Swinging up a pendulum by energy control," Automatica **36**, 287–295 (2000).
[11] M. W. Spong, "The swing up control problem for the acrobot," IEEE Control Syst. Mag. **15**, 49–55 (1995).
[12] Q. Wei, W. P. Dayawansa, and W. S. Levine, "Nonlinear controller for an inverted pendulum having restricted travel," Automatica **31**, 841–850 (1995).
[13] D. M. Alonso, E. E. Paolini, and J. L. Moiola, "Controlling an inverted pendulum with bounded controls," in *Dynamics, Bifurcations, and Control* (Springer, 2002), pp. 3–16.
[14] D. M. Alonso, E. E. Paolini, and J. L. Moiola, "Global bifurcation analysis of a controlled underactuated mechanical system," Nonlinear Dyn. **40**, 205–225 (2005).
[15] A. Pikovsky, J. Kurths, M. Rosenblum, J. Kurths, B. Chirikov, C. U. Press, P. Cvitanovic, F. Moss, and H. Swinney, *Synchronization: A Universal Concept in Nonlinear Sciences*, Cambridge Nonlinear Science Series (Cambridge University Press, 2001).
[16] S. Strogatz, *Sync: The Emerging Science of Spontaneous Order* (Theia, Scranton, 2003).
[17] S. H. Strogatz, D. M. Abrams, A. McRobie, B. Eckhardt, and E. Ott, "Crowd synchrony on the millennium bridge," Nature **438**, 43–44 (2005).
[18] R. E. Mirollo and S. H. Strogatz, "Synchronization of pulse-coupled biological oscillators," SIAM J. Appl. Math. **50**, 1645–1662 (1990).
[19] Y. Kuramoto, "Self-entrainment of a population of coupled non-linear oscillators," in *International Symposium on Mathematical Problems in Theoretical Physics* (Springer, 1975), pp. 420–422.
[20] M. Feldman, *Hilbert Transform Applications in Mechanical Vibration: Feldman/Hilbert Transform Applications in Mechanical Vibration* (Wiley, 2011).
[21] I. Blekhman, "The problem of synchronization of dynamical systems," J. Appl. Math. Mech. **28**, 239–265 (1964).
[22] J. Pena Ramirez, R. H. Fey, and H. Nijmeijer, "Synchronization of weakly nonlinear oscillators with huygens' coupling," Chaos **23**, 033118 (2013).
[23] J. P. Ramirez, K. Aihara, R. Fey, and H. Nijmeijer, "Further understanding of huygens' coupled clocks: The effect of stiffness," Physica D **270**, 11–19 (2014).
[24] A. Pogromsky, V. Belykh, and H. Nijmeijer, "Controlled synchronization of pendula," in *42nd IEEE International Conference on Decision and Control (IEEE Cat. No. 03CH37475)* (IEEE, 2003), Vol. 5, pp. 4381–4386.
[25] J. P. Ramirez, R. C. Garcia, and J. Alvarez, "Synchronization of two inverted pendula via dynamic coupling," in *2016 Australian Control Conference (AuCC)* (IEEE, 2016), pp. 87–92.
[26] J. Gout, M. Quade, K. Shafi, R. K. Niven, and M. Abel, "Synchronization control of oscillator networks using symbolic regression," Nonlinear Dyn. **91**, 1001–1021 (2018).
[27] J. Pantaleone, "Synchronization of metronomes," Am. J. Phys. **70**, 992–1000 (2002).
[28] G. H. Goldsztein, L. Q. English, E. Behta, H. Finder, A. N. Nadeau, and S. H. Strogatz, "Coupled metronomes on a moving platform with coulomb friction," Chaos **32**, 043119 (2022).
[29] J. P. Ramirez, L. A. Olvera, H. Nijmeijer, and J. Alvarez, "The sympathy of two pendulum clocks: Beyond Huygens' observations," Sci. Rep. **6**, 23580 (2016).
[30] P. Koluda, P. Perlikowski, K. Czolczynski, and T. Kapitaniak, "Synchronization of two self-excited double pendula," Eur. Phys. J. Spec. Top. **223**, 613–629 (2014).
[31] W. Ditto and K. Showalter, "Focus issue: Control and synchronization of chaos," Chaos **7**, 509–511 (1997).
[32] H. Nijmeijer, "Control of chaos and synchronization," Syst. Control Lett. **31**, 259–262 (1997).
[33] E. Ott, C. Grebogi, and J. A. Yorke, "Controlling chaos," Phys. Rev. Lett. **64**, 1196–1199 (1990).
[34] M. Rosenblum and A. Pikovsky, "Efficient determination of synchronization domains from observations of asynchronous dynamics," Chaos **28**, 106301 (2018).
[35] D. Dudkowski, J. Wojewoda, K. Czolczynski, and T. Kapitaniak, "Experimental chaotic synchronization for coupled double pendula," Chaos **31**, 061107 (2021).
[36] J. Strzalko, J. Grabski, J. Wojewoda, M. Wiercigroch, and T. Kapitaniak, "Synchronous rotation of the set of double pendula: Experimental observations," Chaos **22**, 047503 (2012).
[37] O. Wale, "Beating in coupled pendulums," Report B.sc. Design Project (University of Cape Town, 2016).
[38] A. Zelman, "Nonstationary dynamics of an inertia wheel pendulum controlled inverted pendulum," Report—B.Sc. Research Project, Mechanical Engineering (Technion—Israel Institute of Technology, 2019).
[39] A. Dhooge, W. Govaerts, and Y. Kuznetsov, "Matcont," ACM Trans. Math. Software **29**, 141–164 (2003).
[40] Y. A. Kuznetsov, I. A. Kuznetsov, and Y. Kuznetsov, *Elements of Applied Bifurcation Theory* (Springer, 1998), Vol. 112.
[41] J. Guckenheimer, M. Myers, and B. Sturmfels, "Computing Hopf bifurcations I," SIAM J. Numer. Anal. **34**, 1–21 (1997).
[42] A. H. Nayfeh, *Perturbation Methods*, Physics Textbook (Wiley-VCH, Weinheim, 2004).
[43] J. J. Thomsen, *Vibrations and Stability* (Springer, 2003), Vol. 2.
[44] Y. Kuramoto and D. Battogtokh, "Coexistence of coherence and incoherence in nonlocally coupled phase oscillators," Nonlinear Phenom. Complex Syst. **5**, 380–385 (2002).
[45] D. M. Abrams, R. Mirollo, S. H. Strogatz, and D. A. Wiley, "Solvable model for chimera states of coupled oscillators," Phys. Rev. Lett. **101**, 084103 (2008).